


 Cite this: *RSC Adv.*, 2026, 16, 2873

# Numerical modeling to enhance the efficiency of experimentally fabricated Sb<sub>2</sub>Se<sub>3</sub>-based solar cell

 Towhid Adnan Chowdhury \*

Remarkable optical and electrical characteristics make antimony selenide (Sb<sub>2</sub>Se<sub>3</sub>) a potential absorber layer for heterojunction solar cells. In this work, a novel heterojunction Sb<sub>2</sub>Se<sub>3</sub>-based thin film solar cell using non-toxic tin sulfide (SnS<sub>2</sub>) as buffer layer instead of toxic cadmium sulfide (CdS) is designed utilizing Solar Cell Capacitance Simulator in one-dimension (SCAPS-1D). To validate the simulation model, the results of experimentally fabricated glass/SnO<sub>2</sub>:F(FTO)/CdS/Sb<sub>2</sub>Se<sub>3</sub>/Au solar cell structure with efficiency of 5.17% is reproduced in SCAPS. SnS<sub>2</sub> buffer layer provides better band alignment with the Sb<sub>2</sub>Se<sub>3</sub> absorber than CdS buffer layer and improves efficiency. The device performance is optimized by altering thickness, doping concentration, bandgap, defect density, interface defect and capture cross-section for the different layers. The maximum efficiency obtained for the optimized FTO/SnS<sub>2</sub>/Sb<sub>2</sub>Se<sub>3</sub>/Au photovoltaic structure is 12.31% when the Sb<sub>2</sub>Se<sub>3</sub> absorber, SnS<sub>2</sub> buffer and FTO layer thickness are optimized at 0.4 μm, 0.03 μm, and 0.1 μm respectively and their doping are optimized at 10<sup>16</sup> cm<sup>-3</sup>, 10<sup>18</sup> cm<sup>-3</sup> and 10<sup>20</sup> cm<sup>-3</sup> respectively. Addition of tin monosulfide (SnS) as back surface field (BSF) layer boosts the efficiency by decreasing carrier recombination and preventing electrons from reaching back contact due to proper band alignment formed at SnS/Sb<sub>2</sub>Se<sub>3</sub> interface. The efficiency of 24.86% with V<sub>OC</sub> = 0.94 V, J<sub>SC</sub> = 31.98 mA cm<sup>-2</sup>, and FF = 83.09% is obtained for the proposed FTO/SnS<sub>2</sub>/Sb<sub>2</sub>Se<sub>3</sub>/SnS/Au photovoltaic structure with SnS BSF layer at thickness of 0.2 μm and doping of 10<sup>20</sup> cm<sup>-3</sup>. Moreover, the impacts of operating temperature, parasitic resistance and back contact work function on the performance parameters of the designed solar cell are analyzed. These findings indicate that non-toxic SnS and SnS<sub>2</sub> can be utilized as a promising BSF and buffer layer respectively to produce cost-effective, environmental friendly and extremely efficient Sb<sub>2</sub>Se<sub>3</sub>-based thin film solar cell.

 Received 20th June 2025  
 Accepted 2nd January 2026

DOI: 10.1039/d5ra04411a

[rsc.li/rsc-advances](http://rsc.li/rsc-advances)

## 1. Introduction

At present, the expeditious exhaustion of fossil fuels because of large-scale industrialization as well as the quick rise in requirement for conventional energy sources has resulted in severe economic and environmental concerns.<sup>1–4</sup> In this respect, solar cell is a promising solution for ecological and sustainable energy generation which can convert sunlight into high-efficient and cost-effective electrical energy.<sup>5–7</sup> The photovoltaic (PV) researchers are introducing different novel concepts of solar-cell architectures and production considering the stability, climate issues, efficacy and cost in terms of industrial production. Thin film solar cells (TFSCs) have achieved widespread attention because of high performance and fast growth among the various types of PV solar cells.<sup>8–10</sup> At present, metallic chalcogenides copper-indium-gallium-selenide (CIGS) and cadmium telluride (CdTe) based TFSCs are considered as promising candidates for electricity generation with efficiency beyond 23%.<sup>11,12</sup> But these absorbers have several disadvantages

such as toxicity, high cost and scarcity.<sup>13,14</sup> Conventional kesterite-based absorbers such as copper zinc tin sulphide selenide (CZTSSe) obtained highest efficiency of 12.6% due to problems of controlling the composition and defects during fabrication.<sup>15</sup> Recently, Sb<sub>2</sub>Se<sub>3</sub>, a binary compound, has displayed superb potential as an absorber layer in TFSC technology.<sup>16–18</sup> It is composed of earth-abundant and less-toxic elements. It has a band gap of 1.1–1.3 eV, long carrier lifetime, a high absorption coefficient over the visible spectrum (>10<sup>5</sup> cm<sup>-1</sup>), low melting point (550 °C) and decent carrier mobility (hole mobility up to 42 cm<sup>2</sup> V<sup>-1</sup> s<sup>-1</sup> and electron mobility above 16.9 cm<sup>2</sup> V<sup>-1</sup> s<sup>-1</sup>).<sup>12,17,19–21</sup> Moreover, benign grain boundary structure of Sb<sub>2</sub>Se<sub>3</sub> makes it a potential absorber material.<sup>22</sup> An efficiency of 0.66% was obtained by Messina *et al.* in 2009 using CdS as a buffer layer.<sup>23</sup> Choi *et al.* and Zhou *et al.* obtained 3.21% and 2.26% efficiency using TiO<sub>2</sub> buffer layer in 2014.<sup>24,25</sup> In 2017, Chen *et al.* and Wang *et al.* achieved 6.5% and 5.93% efficiency with CdS and ZnO buffer layers respectively.<sup>16,18</sup> By employing a vapor-transport method, Wen *et al.* obtained 7.6% efficiency using CdS buffer layer in 2018.<sup>26</sup> In 2019, Li *et al.* obtained highest efficiency of 9.2% using CdS buffer layer for Sb<sub>2</sub>Se<sub>3</sub> based solar cells by junction

Faculty of Department of Electrical & Electronic Engineering, Ahsanullah University of Science & Technology, Dhaka, Bangladesh. E-mail: towhid6789@yahoo.com



interface engineering.<sup>19</sup> In 2021, Guo *et al.* obtained an efficiency of 7.15% by incorporating NiO<sub>x</sub> as back surface field (BSF) layer.<sup>27</sup> Recently, Tang *et al.* have obtained efficiency of 8.64% by sputtering method.<sup>28</sup> In 2022, Dong *et al.* obtained an efficiency of 6.7% by optimizing deep defects containing V<sub>Se</sub> on the Sb<sub>2</sub>Se<sub>3</sub> film.<sup>29</sup> The efficiency of Sb<sub>2</sub>Se<sub>3</sub>-based solar cells still far from the theoretical value of 31% according to Shockley–Queisser limit.<sup>30</sup> Different methods namely electrodeposition, spin coating, sputtering, spray pyrolysis, chemical bath deposition and vacuum evaporation have been employed to achieve high quality Sb<sub>2</sub>Se<sub>3</sub> film.<sup>31</sup> Sb<sub>2</sub>Se<sub>3</sub> has various applications in memory gadgets, solar cells, photodetectors and batteries.<sup>32</sup> To obtain the theoretical efficiency of Sb<sub>2</sub>Se<sub>3</sub> based solar cells, various simulation studies have been performed. Basak *et al.* have obtained efficiency of 12.62% for Sb<sub>2</sub>Se<sub>3</sub>/CdS heterojunction solar cell structure.<sup>33</sup> An efficiency of 13.20% was obtained by Baig *et al.* using CNT/Cu<sub>2</sub>O/Sb<sub>2</sub>Se<sub>3</sub>/In<sub>2</sub>S<sub>3</sub>/ITO photovoltaic architecture.<sup>34</sup> Kumari *et al.* achieved 24% efficiency in Mo/Sb<sub>2</sub>Se<sub>3</sub>/ZnSe/Ag solar cell structure.<sup>17</sup> Mamta *et al.* gained 27.84% efficiency in Sb<sub>2</sub>Se<sub>3</sub>/CdS/ZnO solar cell structure.<sup>35</sup> Ahmed *et al.* obtained 29.35% efficiency for Mo/BaSi<sub>2</sub>/Sb<sub>2</sub>Se<sub>3</sub>/CdS/FTO/Al solar cell architecture.<sup>36</sup> Sunny *et al.* achieved 29.89% efficiency for Al/F:SnO<sub>2</sub>(FTO)/CdS/Sb<sub>2</sub>Se<sub>3</sub>/SnS/Mo solar cell structure.<sup>37</sup>

An ideal buffer layer should have high electrical conductivity, decent carrier mobility and a proper band alignment with minimum conduction band offset (CBO).<sup>38</sup> In experimental Sb<sub>2</sub>Se<sub>3</sub> based solar cell, CdS functions as mostly used buffer layer due to its electrical and chemical stability.<sup>12,39,40</sup> The main problem with CdS is its toxicity which causes human and environmental health issues.<sup>41,42</sup> Moreover, large lattice mismatch and diffusion of S and Cd into the Sb<sub>2</sub>Se<sub>3</sub> film degrades cell performance.<sup>17</sup> Several works have used other buffer layers such as ZnO,<sup>43</sup> TiO<sub>2</sub> (ref. 44) and SnO<sub>2</sub> (ref. 45) instead of CdS layer. The two-dimensional (2D) chalcogenide sulfur (S)-based tin sulfide (SnS<sub>2</sub>) with an appropriate bandgap of 1.82–2.88 eV and a large absorption coefficient of  $\sim 10^5$  cm<sup>-1</sup> is a promising buffer material for producing high-performance solar cells.<sup>46,47</sup> It is cheap, non-toxic and has high electron mobility values of 50 cm<sup>2</sup> V<sup>-1</sup> s<sup>-1</sup>.<sup>48</sup> The wide bandgap of SnS<sub>2</sub> allows loss-free passage of incident light spectrum. Moreover, proper band alignment with absorber layer provides efficient transporting of electrons from absorber layer to the contacts reducing the recombination of holes and electrons and thus boosting the cell efficiency. It can be deposited employing spray pyrolysis, hydrothermal, co-precipitation, chemical vapor deposition (CVD) and chemical bath deposition.<sup>49–52</sup> In this work, SnS<sub>2</sub> is used as a buffer layer for the proposed Sb<sub>2</sub>Se<sub>3</sub> based solar cell.

Ineffective carrier transport and collection by the front and back contacts and carrier recombination at the back contact are the main reasons for poor solar cell efficiency. By inserting the back surface field (BSF) layer between the back contact and absorber layer, the solar cell performance can be enhanced by lowering the surface recombination rate (SRV) and delivering easy transportation of holes to the back electrode by

minimizing the barrier height of the back electrode.<sup>53,54</sup> Many researchers have added inorganic and organic BSF layers such as NiO<sub>x</sub>, Cu<sub>2</sub>O, VO<sub>x</sub>, CZTA, P3HT, PEDOT:PSS, SpiroMeOTAD.<sup>12,34,55–58</sup> Due to toxicity of inorganic BSFs and instability of organic BSFs, researchers are looking for non-toxic and stable BSF layer. In previous studies, inorganic tin monosulfide (SnS) is employed as a BSF layer to reduce carrier recombination at BSF/back contact interface.<sup>37,59,60</sup> It has excellent optoelectronic characteristics such as suitable bandgap of 1.1–1.4 eV, high hole mobility, nontoxicity, cheap and large absorption coefficient ( $>10^4$  cm<sup>-1</sup>).<sup>61–64</sup> Various techniques such as spray pyrolysis, electron beam evaporation, chemical synthesis, sputtering, atomic layer deposition (ALD), thermal evaporation (TE) and vapor transport deposition (VTD) have been used for deposition of SnS films.<sup>62,65–71</sup> In this work, SnS is proposed as BSF layer for Sb<sub>2</sub>Se<sub>3</sub> based TFSC due to its proper band alignment with absorber layer. Though SnS and SnS<sub>2</sub> are used as BSF and buffer layer respectively in previous studies,<sup>37,72</sup> this novel SnO<sub>2</sub>: F(FTO)/SnS<sub>2</sub>/Sb<sub>2</sub>Se<sub>3</sub>/SnS/Au dual-heterojunction (DH) structure using combined use of SnS and SnS<sub>2</sub> as BSF and buffer layer respectively in Sb<sub>2</sub>Se<sub>3</sub> based solar cell has never been simulated to the best of my knowledge. The reason for high efficiency and light trapping of DH solar cell has been achieved as a result of the longer wavelength photon absorption in the p<sup>+</sup>-SnS BSF layer through a tail-states assisted (TSA) two-steps photon upconversion phenomenon. Most previous studies have explored on single absorber structures, overlooking the promising efficiency enhancements obtained by dual absorber layer architectures. There is also limited research on how such dual-heterojunction structures effect efficiency and carrier transport mechanisms in thin film solar cells. The present study aims to systematically explore a novel thin-film solar cell architecture comprising Sb<sub>2</sub>Se<sub>3</sub>, SnS<sub>2</sub> and SnS as absorber, buffer and BSF layer respectively to examine how such an architecture can enhance solar cell performance while eliminating toxic element dependency, thereby bestowing to both material sustainability and technological evolution in next-generation solar cells.

In this present work, a numerical modeling is applied employing SCAPS-1D software to compare simulation results with experimental findings of glass/SnO<sub>2</sub>:F(FTO)/CdS/Sb<sub>2</sub>Se<sub>3</sub>/Au solar cell structure by Li *et al.*<sup>73</sup> After that, toxic CdS is replaced with non-toxic SnS<sub>2</sub> buffer layer which boosts device performance. Then investigation is performed by tuning thickness, doping density, bandgap, defect density and capture cross section of different layers to boost efficiency of proposed cell. Afterwards, SnS is inserted as BSF layer and its physical parameters are optimized to enhance device performance. Finally, the influence of back contact work function, temperature and series and shunt resistance on electrical parameters such as open circuit voltage (V<sub>OC</sub>), short-circuit current density (J<sub>SC</sub>), fill factor (FF) and efficiency (η) of proposed cell is also analyzed. The proposed architecture has the potential to notably enhance the stability and performance of Sb<sub>2</sub>Se<sub>3</sub> based photovoltaic by enhancing the carrier collection and decreasing the back surface recombination.



## 2. Numerical simulation and methodology

### 2.1 Simulation methodology and device architecture

To analyze the proposed glass/FTO/SnS<sub>2</sub>/Sb<sub>2</sub>Se<sub>3</sub>/SnS/Au photovoltaic, the one-dimensional Solar Cell Capacitance Simulator (SCAPS) software version 3.3.09 is applied for numerical simulations. SCAPS-1D application was invented at the Department of Electronics and Information Systems of the University of Ghent, Belgium. There are several other programs to model and simulate solar cell characteristics depending on the device's input hierarchy, including SILVACO ATLAS, COMSOL, AMPS, AFORS-HET, PECSIM and Wx-AMPS.<sup>74,75</sup> However, most of them require expensive licensing fees and high computational resources, making them rarely available for quick device optimization and design. But SCAPS software has many advantages compared to others including the potential to carry out performance examination across up to seven levels, in depth and batch analyses, and simple findings to comprehend and investigate.<sup>76</sup> It is the best accurate non-commercial tool with friendly dialog box, straightforward in operation and supports multi-junction solar cells.<sup>77</sup> Interestingly, the SCAPS-1D is available cost-free and provides results that matches with experimental findings. It is designed to simulate and model solar cells with a heterojunction and homojunction. Thus, providing it a significant edge over the other solar cell simulators. It incorporates complicated simulations of carrier transport, recombination, generation, defects and interface impacts in solar cells which makes it effective and reliable for simulation of photovoltaic devices.<sup>78</sup> All input files that are provided in SCAPS are user-accessible text files, for example the spectral data. Moreover, it is very fast which other programs may lag significantly and the incorporation of metal contacts, shunt resistance, series resistance, capacitance and frequency response and capacitance and voltage relation make this software robust.<sup>79</sup> It has been extensively validated across solar cell research community and different material systems, highlighting its predictive correctness and reliability.<sup>80</sup> Thus, the present research is carried out using the SCAPS-1D simulation tool. It is applied to predict and analyze the optoelectronic parameters of solar cell architectures such as open circuit voltage ( $V_{OC}$ ), short-circuit current density ( $J_{SC}$ ), fill factor (FF) and efficiency ( $\eta$ ) by dealing fundamental equations such as drift-diffusion equation, Poisson's equation and carrier continuity equation.<sup>81</sup> These equations are numerically solved in one dimension by this program.

Fig. 1a depicts the Sb<sub>2</sub>Se<sub>3</sub> baseline superstrate glass/SnO<sub>2</sub>:F(FTO)/CdS/Sb<sub>2</sub>Se<sub>3</sub>/Au solar cell structure manufactured experimentally by Li *et al.* implementing close-space sublimation (CSS) method which provides higher quality of Sb<sub>2</sub>Se<sub>3</sub> absorber film deposition and improved device heterojunctions due to independent control of the substrate and source temperatures.<sup>73</sup> Fig. 1b illustrates proposed glass/FTO/SnS<sub>2</sub>/Sb<sub>2</sub>Se<sub>3</sub>/SnS/Au photovoltaic architecture for the maximum efficiency that is the objective of this article. A p-type Sb<sub>2</sub>Se<sub>3</sub> absorber layer, n-type SnS<sub>2</sub> buffer, and FTO (fluorine-doped tin oxide) window

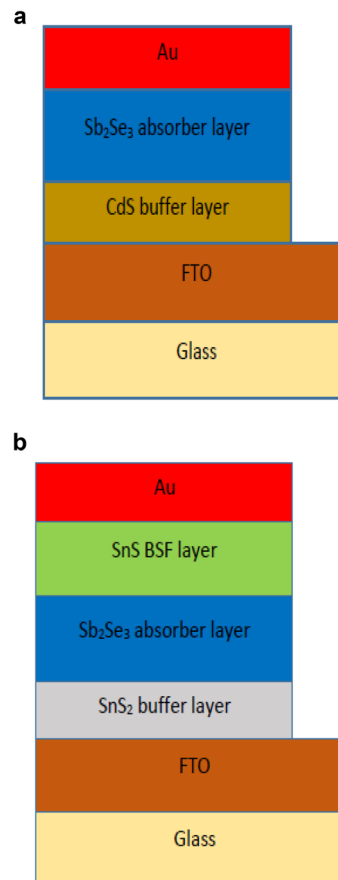


Fig. 1 (a). Schematic diagram of the reference glass/FTO/CdS/Sb<sub>2</sub>Se<sub>3</sub>/Au solar cell. (b) Schematic diagram of the proposed glass/FTO/SnS<sub>2</sub>/Sb<sub>2</sub>Se<sub>3</sub>/SnS/Au solar cell.

layer compose the proposed solar cell. Moreover, SnS is added as the BSF layer to boost efficiency. FTO and gold (Au) are used as front and back contacts respectively. Table 1 represents material parameters applied in the proposed Sb<sub>2</sub>Se<sub>3</sub>-based photovoltaic with BSF layer obtained from both simulation and practical works. In order to find equality between experimental and simulation findings, bulk layers and absorber/buffer interface are incorporated with defects. The interfacial defect and contact parameters applied in this work are listed in Tables 2 and 3 respectively. To reproduce experimental results, the BSF layer is not inserted in the initial section of simulation. The simulation study has been performed under AM 1.5 G spectral irradiation (100 mW cm<sup>-2</sup>) at 300 K. Moreover, the absorption coefficient  $\alpha(\lambda)$  for films is obtained using the new modified  $E_g$ -sqrt model, which is an updated version of the traditional sqrt ( $h\nu - E_g$ ) model. The "Tauc law" demonstrates this relationship as illustrated in eqn (1).

$$\alpha(\lambda) = \left( \alpha_0 + \beta_0 \frac{E_g}{h\nu} \right) \sqrt{\frac{h\nu}{E_g} - 1} \quad (1)$$

Here,  $\alpha(\lambda)$  represents the optical absorption coefficient as a function of wavelength ( $\lambda$ ) or photon energy ( $h\nu$ ) and  $E_g$  denotes the bandgap. Eqn (2) and (3) relate the model constants



Table 1 Material parameters employed for simulating Sb<sub>2</sub>Se<sub>3</sub> based thin film solar cell

Parameter	Sb <sub>2</sub> Se <sub>3</sub> (ref. 20)	CdS <sup>20</sup>	SnS <sub>2</sub> (ref. 5)	FTO <sup>20</sup>	SnS <sup>86</sup>
Absorption co-efficient ( $\alpha$ ) (cm <sup>-1</sup> )	SCAPS	SCAPS	SCAPS	SCAPS	SCAPS
Thickness ( $\mu$ m)	0.54	0.05	0.05	0.5	0.1
Bandgap (eV)	1.03	2.4	2.24	3.6	1.2
Electron affinity (eV)	4.15	4.0	4.2	4.0	4.2
Dielectric permittivity	14.5	10	10	9	13
CB effective density of states (cm <sup>-3</sup> )	$8 \times 10^{17}$	$2.2 \times 10^{18}$	$2.2 \times 10^{18}$	$2.2 \times 10^{18}$	$1.18 \times 10^{18}$
VB effective density of states (cm <sup>-3</sup> )	$1.8 \times 10^{19}$	$1.8 \times 10^{19}$	$1.8 \times 10^{19}$	$1.8 \times 10^{19}$	$4.76 \times 10^{18}$
Electron thermal velocity (cm s <sup>-1</sup> )	$1 \times 10^7$	$1 \times 10^7$	$1 \times 10^7$	$1 \times 10^7$	$1 \times 10^7$
Hole thermal velocity (cm <sup>-1</sup> )	$1 \times 10^7$	$1 \times 10^7$	$1 \times 10^7$	$1 \times 10^7$	$1 \times 10^7$
Electron mobility (cm <sup>2</sup> V <sup>-1</sup> s <sup>-1</sup> )	15	80	50	20	30
Hole mobility (cm <sup>2</sup> V <sup>-1</sup> s <sup>-1</sup> )	15	25	50	10	90
Shallow uniform donor density, N <sub>D</sub> (cm <sup>-3</sup> )	0	$1 \times 10^{18}$	$1 \times 10^{18}$	$1 \times 10^{17}$	0
Shallow uniform acceptor density, N <sub>A</sub> (cm <sup>-3</sup> )	$1 \times 10^{13}$	0	0	0	$1 \times 10^{18}$
Defect type	Donor	Acceptor	Acceptor	Donor	Donor
Energetic distribution	Single	Single	Single	Single	Single
Capture cross section of electrons (cm <sup>2</sup> )	$2.3 \times 10^{-11}$	$1.5 \times 10^{-12}$	$1.5 \times 10^{-12}$	$1 \times 10^{-12}$	$1 \times 10^{-15}$
Capture cross section of holes (cm <sup>2</sup> )	$4.39 \times 10^{-11}$	$1.5 \times 10^{-12}$	$1.5 \times 10^{-12}$	$1 \times 10^{-14}$	$1 \times 10^{-15}$
Defect density, N <sub>t</sub> (cm <sup>-3</sup> )	$1 \times 10^{13}$	$1 \times 10^{18}$	$1 \times 10^{15}$	$1 \times 10^{16}$	$1 \times 10^{14}$

$\alpha_0$  and  $\beta_0$  to the conventional model constants A and B as illustrated below:

$$\alpha_0 = A\sqrt{E_g} \quad (2)$$

$$\beta_0 = \frac{B}{\sqrt{E_g}} \quad (3)$$

The material absorption spectra is produced automatically depending on the  $\sqrt{E_g}$  model and the input parameters supplied, including A and B in SCAPS-1D.<sup>82,83</sup> The sub-bandgap absorption impact on solar cell performance is automatically accounted by SCAPS software once the optical data are supplied. Conversely, there are limitations of SCAPS. One of its limitations is that it can provide imprecision results if applied to complex structures or long simulation times because it uses a simplified optical model. It can overestimate the incident light intensity that generates charge due to its inability to account automatically reflection losses that is present at intermediate

interfaces. Additionally, there is an uncertain illustration for a secondary barrier or n-p (rather than p-n) junction.<sup>75</sup> Nano-structural characteristics or plasmonic impacts are some vital light-management methods that are not precisely simulated by it.<sup>84</sup> It is required to incorporate wavelength-dependent complex refractive index ( $n-k$ ) values for materials in SCAPS to increase the simulation correctness.<sup>80,85</sup> Despite these limitations, SCAPS is still advantageous due to its ability to produce results close to experimental findings and its flexible configurations.

## 2.2 Methodology for optimizing solar cell performance parameters

At first, the parameters listed in Tables 1–3 are used to produce solar cell performance parameters that matches experimental findings to validate the simulation model in this research. Afterwards, 15 steps are carried out to obtain optimal values based on varied parameters listed in Tables 1–3. The optimized

Table 2 Interface defect parameters used in simulation

Parameters	Sb <sub>2</sub> Se <sub>3</sub> /CdS	Sb <sub>2</sub> Se <sub>3</sub> /SnS <sub>2</sub>	Sb <sub>2</sub> Se <sub>3</sub> /SnS
Defect type	Neutral	Neutral	Neutral
Energetic distribution	Single	Single	Single
Capture cross section of electrons/holes (cm <sup>2</sup> )	$1 \times 10^{-10}$	$1 \times 10^{-10}$	$1 \times 10^{-19}$
Defect density, N <sub>t</sub> (cm <sup>-2</sup> )	$5 \times 10^{17}$	$5 \times 10^{17}$	$1 \times 10^{10}$

Table 3 Contact parameters used in simulation

Parameter	Back contact	Front contact
Work function	5.1 eV	4.4 eV
Surface recombination velocity of holes (cm s <sup>-1</sup> )	$1 \times 10^7$	$1 \times 10^7$
Surface recombination velocity of electrons (cm s <sup>-1</sup> )	$1 \times 10^7$	$1 \times 10^7$



result obtained in each step is used for the reference cell for the next step.

Step 1: except for the thickness of  $\text{Sb}_2\text{Se}_3$  absorber layer that is varied from 0.1  $\mu\text{m}$  to 1.5  $\mu\text{m}$ , the rest of the parameters are kept constant.

Step 2: the optimum thickness of  $\text{Sb}_2\text{Se}_3$  from the previous step is used as a constant parameter in this step and the carrier density of this layer is changed from  $10^{12}$ – $5 \times 10^{16} \text{ cm}^{-3}$ .

Step 3: the defect density of  $\text{Sb}_2\text{Se}_3$  is varied in the range of  $10^{10}$ – $10^{15} \text{ cm}^{-3}$  to study its impact on optimized cell obtained in the previous step.

Step 4: in this step, the bandgap of  $\text{Sb}_2\text{Se}_3$  in the range of 1–1.3 eV is investigated to study its impact on the proposed cell performance.

Step 5: after optimizing the  $\text{Sb}_2\text{Se}_3$  absorber layer, the thickness of  $\text{SnS}_2$  buffer layer is varied from 0.01  $\mu\text{m}$  to 0.1  $\mu\text{m}$  to study its impact on device performance.

Step 6: the impact of  $\text{SnS}_2$  buffer layer carrier density on the photovoltaic parameters of the optimized cell in the previous step is studied by varying it between  $10^{13} \text{ cm}^{-3}$  and  $10^{18} \text{ cm}^{-3}$ .

Step 7: the defect density of the  $\text{SnS}_2$  layer is varied between  $10^{10} \text{ cm}^{-3}$  and  $10^{18} \text{ cm}^{-3}$  while the rest parameters are kept at their optimum values.

Step 8: the effect of FTO window layer thickness is investigated in the range of 0.1–0.6  $\mu\text{m}$ .

Step 9: the carrier concentration of FTO layer is explored in the range of  $10^{17}$ – $10^{20} \text{ cm}^{-3}$  to optimize its value.

Step 10: the impact of  $\text{Sb}_2\text{Se}_3/\text{SnS}_2$  interface defect on performance parameters of the proposed cell is explored in the defect density range of  $10^7$ – $10^{18} \text{ cm}^{-2}$ .

Step 11: the capture cross-section of electron and hole of the  $\text{Sb}_2\text{Se}_3$  layer is varied between  $10^{-19} \text{ cm}^{-2}$  and  $10^{-9} \text{ cm}^{-2}$  while the rest parameters are kept at their optimum values.

Step 12: in this step, the impact of the capture cross-section of electron and hole of the  $\text{Sb}_2\text{Se}_3/\text{SnS}_2$  interface layer is explored to study its impact on performance parameters of optimized cell in the previous step in the range of  $10^{-20}$ – $10^{-8} \text{ cm}^{-2}$ .

Step 13: after optimizing  $\text{Sb}_2\text{Se}_3$ ,  $\text{SnS}_2$  and FTO layer, the thickness of  $\text{SnS}$  BSF layer is changed from 0.02  $\mu\text{m}$  to 0.2  $\mu\text{m}$  to optimize its value.

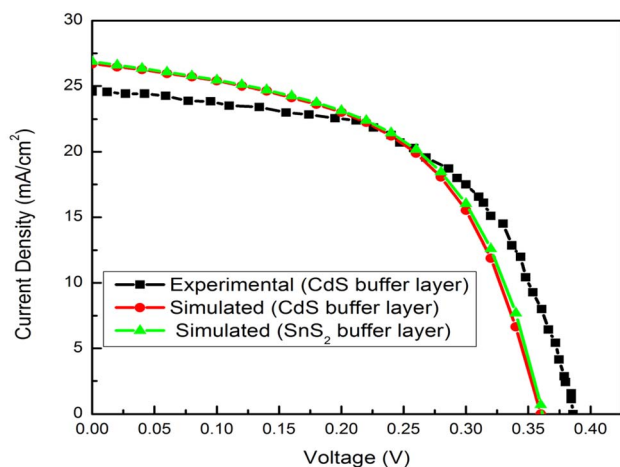
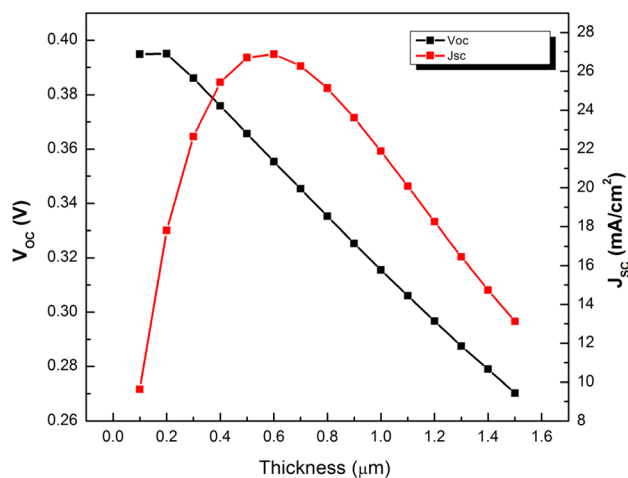


Fig. 2 Comparison of experimental and simulated  $J$ – $V$  curves of  $\text{Sb}_2\text{Se}_3$ -based solar cells.

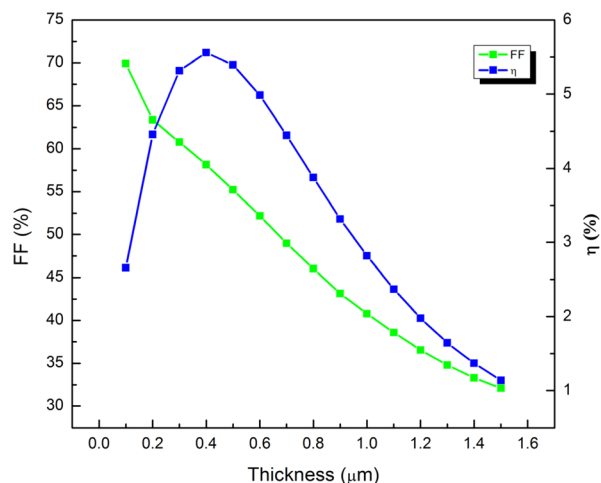


Fig. 3 Impact of  $\text{Sb}_2\text{Se}_3$  absorber layer thickness on solar cell electrical parameters.

Table 4 Comparison of electrical parameters of  $\text{Sb}_2\text{Se}_3$ -based photovoltaic

Solar cell	$V_{OC}$ (V)	$J_{SC}$ ( $\text{mA cm}^{-2}$ )	FF (%)	$\eta$ (%)
Experimental <sup>73</sup>	0.386	24.6	54.5	5.17
Simulated <sup>20</sup>	0.362	27.51	51.95	5.17
Simulated (this work) (CdS buffer layer)	0.358	26.71	54.05	5.17
Simulated (this work) ( $\text{SnS}_2$ buffer layer)	0.362	26.89	54.02	5.25



Step 14: the acceptor concentration of SnS layer is investigated in the range of  $10^{15}$ – $10^{20}$   $\text{cm}^{-3}$  to study its impact on device output.

Step 15: to optimize defect density in SnS BSF layer, defect density is investigated in the range of  $10^{10}$ – $10^{20}$   $\text{cm}^{-3}$  in this last step.

Finally, the effect of back contact work function (4.5–5.4 eV), temperature (300–400 K), series resistance ( $0$ – $8$   $\Omega$   $\text{cm}^2$ ) and shunt resistance ( $200$ – $1600$   $\Omega$   $\text{cm}^2$ ) on the optimized cell is explored.

### 3. Results and analysis

#### 3.1 Validation and comparison of simulation model

The reproduced, experimental and proposed current density–voltage characteristics of the  $\text{Sb}_2\text{Se}_3$  based photovoltaic are compared, as depicted in Fig. 2. Table 4 displays the obtained

performance parameters of simulation results in consideration with experimental outcomes. The device outputs including  $V_{\text{OC}}$  of  $0.358$  V,  $J_{\text{SC}}$  of  $26.71$   $\text{mA cm}^{-2}$ , FF  $54.05\%$ , and efficiency of  $5.17\%$  are achieved from the simulated  $J$ – $V$  characteristics with CdS buffer layer by neglecting series and shunt resistances. On the contrary, the efficiency of  $5.17\%$  with  $V_{\text{OC}}$  of  $0.386$  V,  $J_{\text{SC}}$  of  $24.6$   $\text{mA cm}^{-2}$ , and FF  $54.5\%$  is found for the experimental  $\text{Sb}_2\text{Se}_3$  based photovoltaic.<sup>73</sup> The approximately same result obtained from the experimental and simulation works validates this simulation model. To limit extreme illumination instability due to the diffusion of  $\text{Cd}^{2+}$  from the buffer layer and toxicity of CdS buffer layer, non-toxic  $\text{SnS}_2$  is used as a buffer layer in this simulation work.<sup>73</sup> An efficiency of  $5.25\%$  with  $V_{\text{OC}}$  of  $0.362$  V,  $J_{\text{SC}}$  of  $26.89$   $\text{mA cm}^{-2}$ , and FF  $53.99\%$  is obtained for the proposed  $\text{Sb}_2\text{Se}_3$  based photovoltaic with  $\text{SnS}_2$  as a buffer layer. The result indicates that  $\text{SnS}_2$  can be used as a novel buffer layer for  $\text{Sb}_2\text{Se}_3$  based reference solar cell instead of toxic CdS buffer

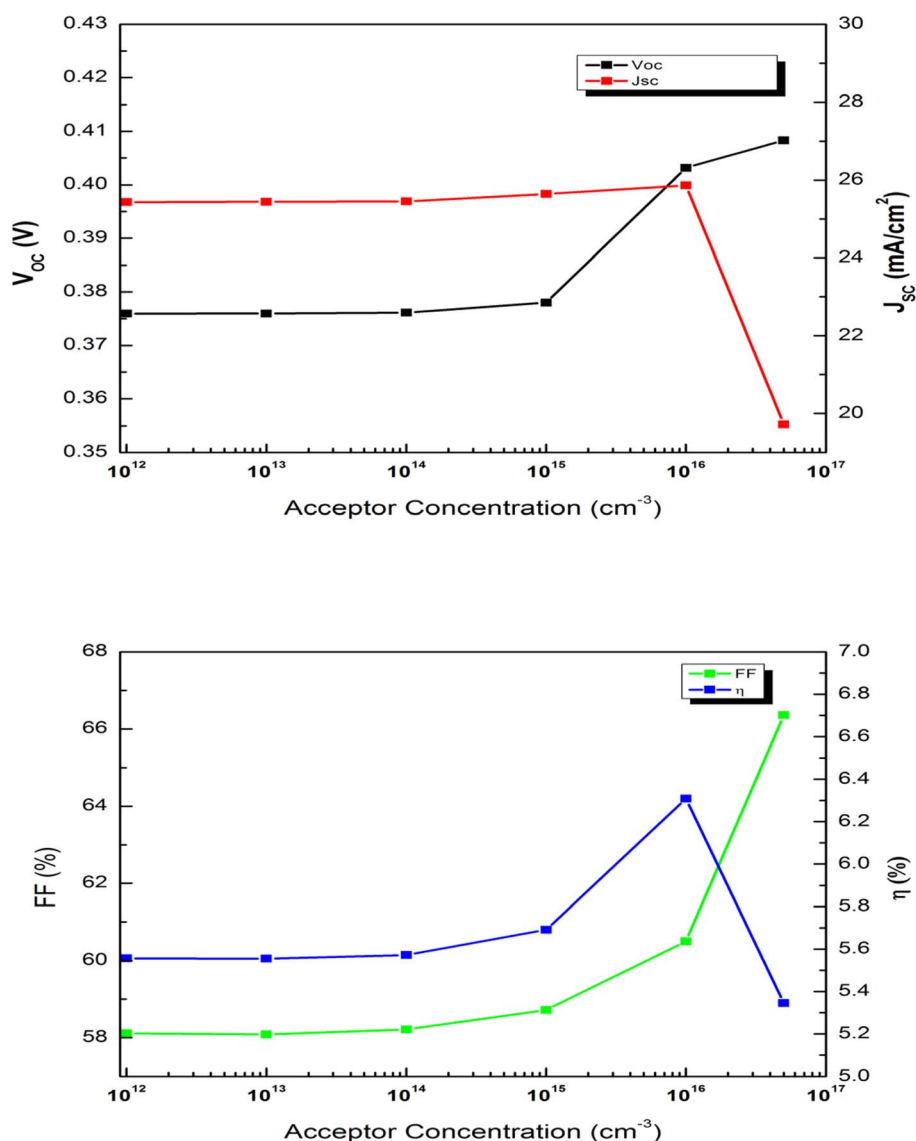


Fig. 4 Impact of  $\text{Sb}_2\text{Se}_3$  absorber layer acceptor concentration on device performance.



layer as it provides better efficiency. As a result,  $\text{SnS}_2$  is used as a buffer layer for  $\text{Sb}_2\text{Se}_3$  based reference photovoltaic in this simulation study.

### 3.2 Impact of $\text{Sb}_2\text{Se}_3$ absorber layer thickness

An optimal absorber layer thickness ensures that photo-generated electron-hole pairs reach their respective contacts without recombination. The influence of the  $\text{Sb}_2\text{Se}_3$  absorber layer thickness is examined by tuning absorber layer thickness from 0.1–1.5  $\mu\text{m}$ , while different layers material parameters are kept unchanged. Solar cell output corresponding to absorber layer thickness variation are shown in Fig. 3. It is observed that  $J_{\text{SC}}$  increases from 9.63  $\text{mA cm}^{-2}$  to 26.88  $\text{mA cm}^{-2}$  as absorber layer thickness is increased from 0.1–0.6  $\mu\text{m}$  due to increase in

electron-hole pair generation. Afterwards it starts decreasing due to recombination and reaches 13.13  $\text{mA cm}^{-2}$  as absorber layer thickness is enhanced to 1.5  $\mu\text{m}$ .  $V_{\text{OC}}$  remains almost constant at 0.395 V as absorber layer thickness is enhanced from 0.1–0.2  $\mu\text{m}$ . Then, it starts decreasing due to recombination and reaches 0.27 V as absorber layer thickness is enhanced to 1.5  $\mu\text{m}$ .<sup>87,88</sup> FF decreases from 69.9–32.1% because of rise in series resistance as absorber layer thickness is increased from 0.1–1.5  $\mu\text{m}$ . The combined impact of FF,  $V_{\text{OC}}$  and  $J_{\text{SC}}$  cause efficiency to rise from 2.66–5.56% as absorber layer thickness is increased from 0.1–0.4  $\mu\text{m}$ . Then efficiency starts to decline as absorber layer thickness is increased and reaches 1.14% as absorber layer thickness is enhanced to 1.5  $\mu\text{m}$ . A thin absorber layer results in low both  $J_{\text{SC}}$  and efficiency due to reduction of absorption capacity of light. Enhancement of absorber layer

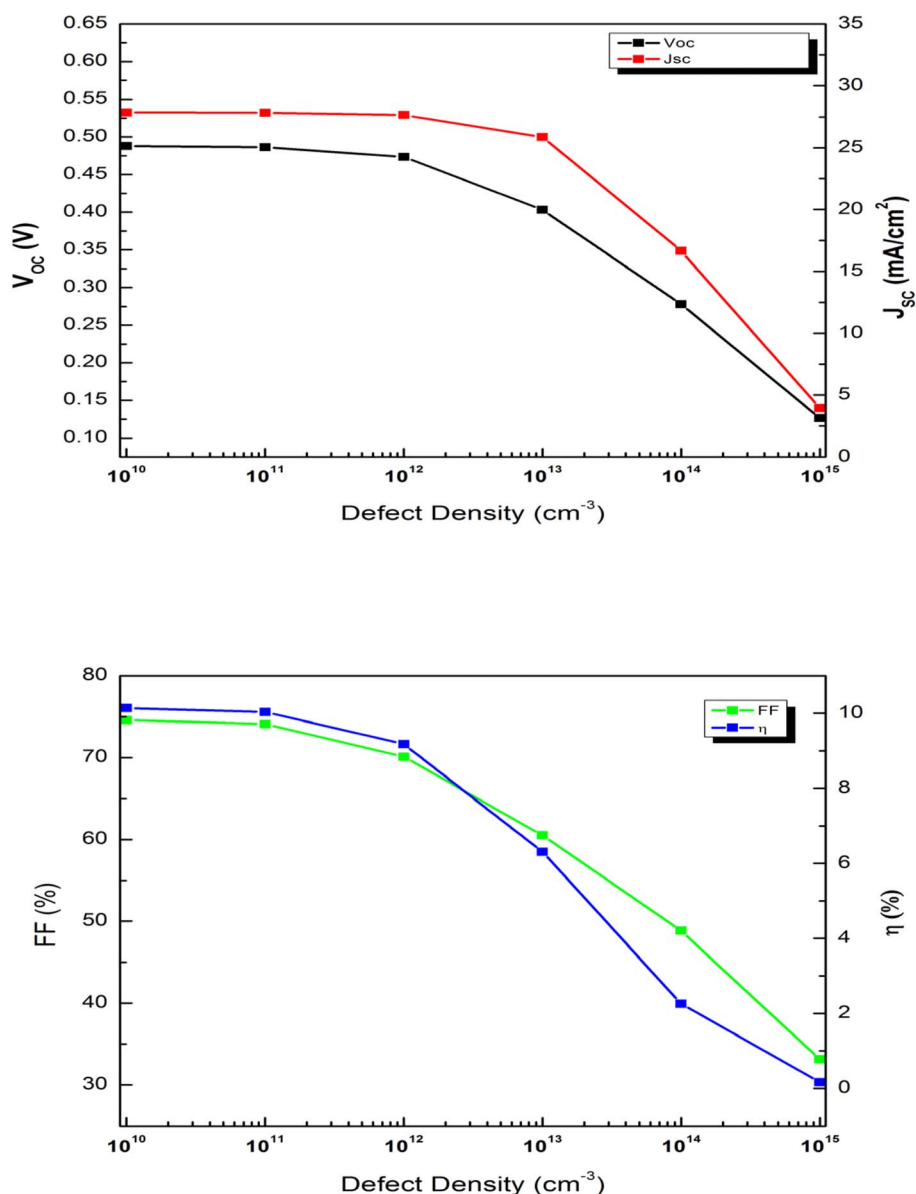


Fig. 5 Impact of  $\text{Sb}_2\text{Se}_3$  absorber layer defect density on solar cell output.



thickness increases efficiency of the solar cell due to large number of photons being absorbed and rise in carrier generation.<sup>14</sup> Efficiency declines as absorber layer thickness is enhanced above  $0.4\ \mu\text{m}$  due to recombination as the path length covered by photo-generated carriers become very large.<sup>89</sup> So absorber layer thickness is optimized at  $0.4\ \mu\text{m}$  which falls within range published in previous works.<sup>12,34</sup>

### 3.3 Influence of $\text{Sb}_2\text{Se}_3$ absorber layer carrier density

The effect of the  $\text{Sb}_2\text{Se}_3$  absorber layer carrier density on device output is examined and simulation outcomes are displayed in Fig. 4. The  $\text{Sb}_2\text{Se}_3$  absorber layer acceptor density is tuned from  $10^{12}$ – $5 \times 10^{16}\ \text{cm}^{-3}$ .  $V_{\text{OC}}$  increases from 0.38 V to 0.41 V and FF rises from 58.12–66.36% as absorber layer acceptor concentration is increased in considered range.  $J_{\text{SC}}$  increases slightly from

$25.43\ \text{mA cm}^{-2}$  to  $25.86\ \text{mA cm}^{-2}$  as doping density is tuned from  $10^{12}$ – $10^{16}\ \text{cm}^{-3}$  after which it starts decreasing. An enhanced doping density results in rise in the bulk and interface recombination rate, thereby declining  $J_{\text{SC}}$ .<sup>54</sup> The combined effect of  $V_{\text{OC}}$ ,  $J_{\text{SC}}$  and FF causes efficiency to rise from 5.56–6.31% with increase in acceptor concentration from  $10^{12}$ – $10^{16}\ \text{cm}^{-3}$ . Afterwards, efficiency degrades. Increase in the carrier density creates the built-in potential at the interface which decreases the recombination and rises the efficiency up to a certain limit.<sup>90</sup> Additional hole recombination centers created at high doping density in the absorber due to increased acceptor impurity increase recombination and declines efficiency.<sup>14</sup> So the optimal absorber layer doping density chosen is  $10^{16}\ \text{cm}^{-3}$  which is within doping concentration value used in previous works.<sup>12,37</sup>

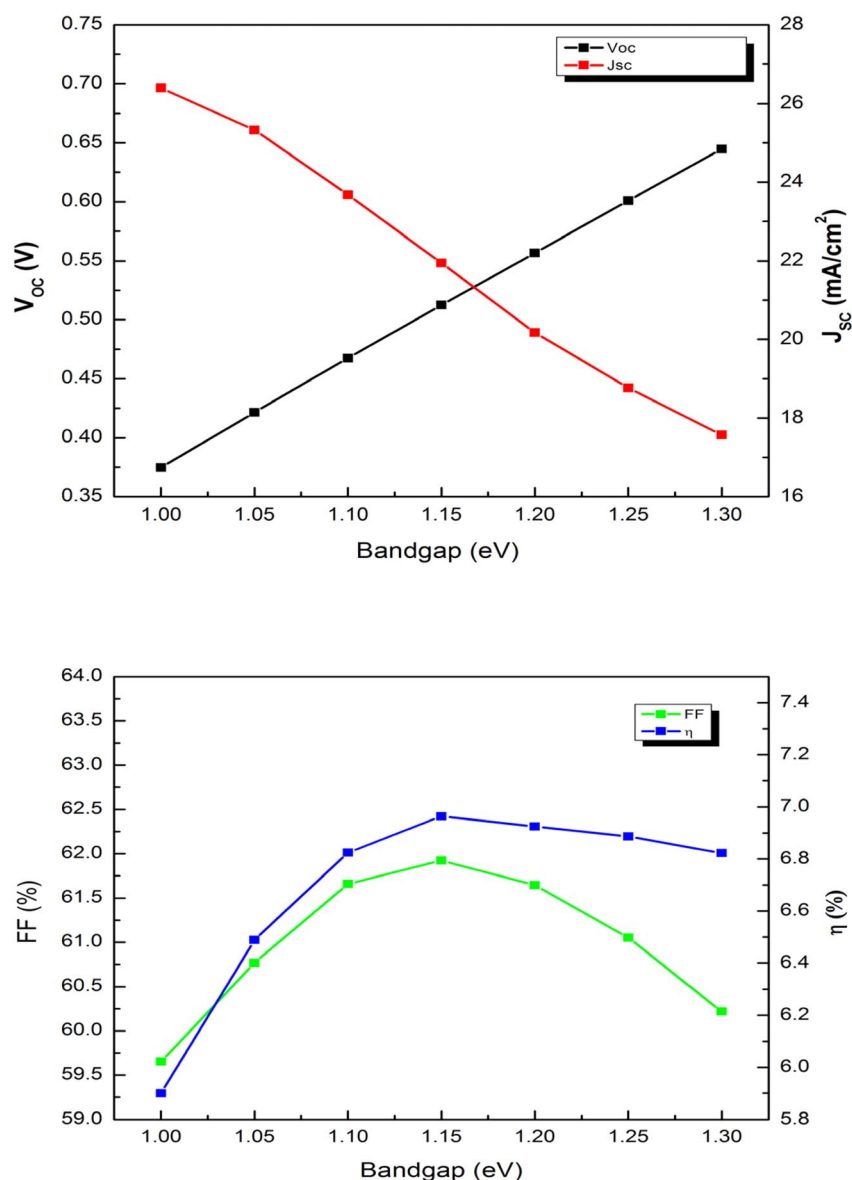


Fig. 6 Solar cell characteristics with respect to  $\text{Sb}_2\text{Se}_3$  absorber layer bandgap.



### 3.4 Effect of $\text{Sb}_2\text{Se}_3$ absorber layer defect density

The defect density of the absorber layer which are inevitable during the fabrication plays a vital role in impacting the performance of solar cells. Defects in the absorber layer results from antisite defects, point defects, crystal imperfections and interstitials. The effect of the  $\text{Sb}_2\text{Se}_3$  absorber layer defect density is examined and outcomes are depicted in Fig. 5. The  $\text{Sb}_2\text{Se}_3$  absorber layer defect density is altered from  $10^{10}$ – $10^{15} \text{ cm}^{-3}$ . Both  $V_{\text{OC}}$  and  $J_{\text{SC}}$  remain almost fixed up to defect density of  $10^{12} \text{ cm}^{-3}$ . Thereafter, both decline significantly as defect density is increased in considered range. FF and  $\eta$  remain unaltered as defect density is increased from  $10^{10}$ – $10^{11} \text{ cm}^{-3}$ . Then both decrease significantly. It is observed that  $J_{\text{SC}}$ ,  $V_{\text{OC}}$ , FF and  $\eta$  decrease from  $27.86 \text{ mA cm}^{-2}$  to  $3.94 \text{ mA cm}^{-2}$ ,  $0.49 \text{ V}$  to  $0.126 \text{ V}$ ,  $74.58$ – $33.13\%$ , and  $10.14$ – $0.16\%$  respectively as defect density is increased from  $10^{10}$ – $10^{15} \text{ cm}^{-3}$ . Increase in absorber layer defect density causes increase in Shockley Read Hall (SRH) recombination of carriers which reduces the carrier lifetime and diffusion length.<sup>14,91,92</sup> As a result, the production of electron–hole is reduced due to prevention of the carriers from reaching the junctions which degrades the solar cell performance parameters.<sup>93</sup> The absorber layer defect density selected is  $10^{13} \text{ cm}^{-3}$  for maximum efficiency which is in good agreement with research works.<sup>17,53</sup>

### 3.5 Optimization of $\text{Sb}_2\text{Se}_3$ absorber layer bandgap

The effect of the  $\text{Sb}_2\text{Se}_3$  absorber layer bandgap is examined by altering absorber layer bandgap from 1–1.3 eV. Solar cell output parameter changes corresponding to absorber layer bandgap variation are depicted in Fig. 6. It is observed that  $J_{\text{SC}}$  decreases from  $26.4 \text{ mA cm}^{-2}$  to  $17.57 \text{ mA cm}^{-2}$  as bandgap rises from 1 to 1.3 eV.  $V_{\text{OC}}$  increases from  $0.375 \text{ V}$  to  $0.64 \text{ V}$  with rise in bandgap in considered range due to decline in radiative recombination rate.<sup>94</sup> Both FF and  $\eta$  rise up to bandgap of  $1.15 \text{ eV}$ . Afterwards, both degrade with rise in bandgap. The generated rate of carriers is enhanced due to improved absorber/buffer junction which causes efficiency to increase as bandgap rises from 1 to  $1.15 \text{ eV}$ .<sup>95</sup> The mismatch between  $\text{Sb}_2\text{Se}_3$  and  $\text{SnS}_2$  bandgap creates recombination centers which increases carriers' recombination with further increase of  $\text{Sb}_2\text{Se}_3$  bandgap above  $1.15 \text{ eV}$  and declines efficiency.<sup>96</sup> So the absorber layer bandgap is optimized at  $1.15 \text{ eV}$  at which  $\eta$  reaches  $6.96\%$ .

### 3.6 Effect of $\text{SnS}_2$ buffer layer thickness

The influence of  $\text{SnS}_2$  buffer layer thickness on solar cell output parameters is also explored. The thickness is tuned from  $0.01$ – $0.1 \mu\text{m}$ . Fig. 7 displays the simulation findings obtained. It is observed that both  $V_{\text{OC}}$  and  $J_{\text{SC}}$  decrease and FF remains almost constant as buffer layer thickness is enhanced in considered range. The photo-generated carriers need to travel longer distance to go to the active region with the rise in the thickness of buffer layer which increases the recombination rate which in turn decreases both  $J_{\text{SC}}$  and  $V_{\text{OC}}$ .<sup>97</sup> The efficiency decreases from  $7.34$ – $6.6\%$  as buffer layer thickness is varied from  $0.01$ – $0.1 \mu\text{m}$ .

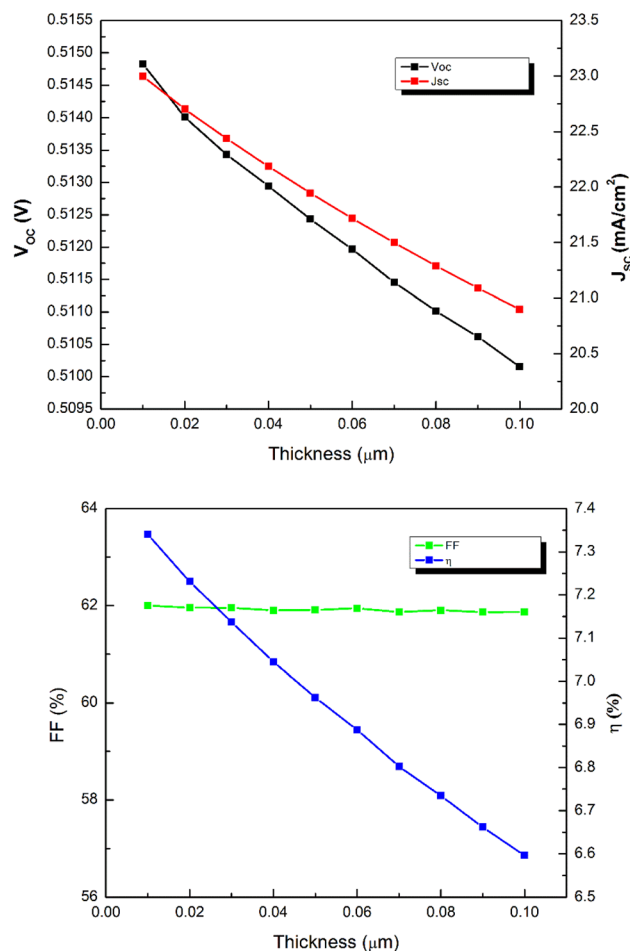


Fig. 7 Impact of  $\text{SnS}_2$  buffer layer thickness on cell performance parameters.

Less number of photons reach the  $\text{Sb}_2\text{Se}_3$  layer which led to reduction of the production of electron–hole pair with increase in the thickness of  $\text{SnS}_2$  layer due to the increase in absorption of photons in the buffer layer which declines efficiency.<sup>93</sup> When the  $\text{SnS}_2$  layer is very thin, the space charge width of the junction is decreased and the pinholes might be created so that  $\text{Sb}_2\text{Se}_3$  directly connects to the front contact.<sup>20</sup> So the optimal buffer layer thickness chosen is  $0.03 \mu\text{m}$  which is also used in published researches.<sup>98,99</sup>

### 3.7 Influence of $\text{SnS}_2$ buffer layer donor density

The effect of the  $\text{SnS}_2$  buffer layer donor concentration is examined and simulation findings are displayed in Fig. 8. The  $\text{SnS}_2$  buffer layer donor density is altered from  $10^{13}$ – $10^{18} \text{ cm}^{-3}$ . FF declines as donor density is enhanced in considered range.  $V_{\text{OC}}$  and  $J_{\text{SC}}$  increase from  $0.45 \text{ V}$  to  $0.51 \text{ V}$  and  $15.36 \text{ mA cm}^{-2}$  to  $22.44 \text{ mA cm}^{-2}$  respectively which causes  $\eta$  to rise from  $5.86$ – $7.14\%$  as buffer layer carrier density is enhanced from  $10^{13}$ – $10^{18} \text{ cm}^{-3}$ . At low carrier concentration, the depletion region extends out of the buffer layer thickness and the diode behavior of the device is decreased.<sup>48</sup> The electric field on the  $\text{Sb}_2\text{Se}_3/\text{SnS}_2$



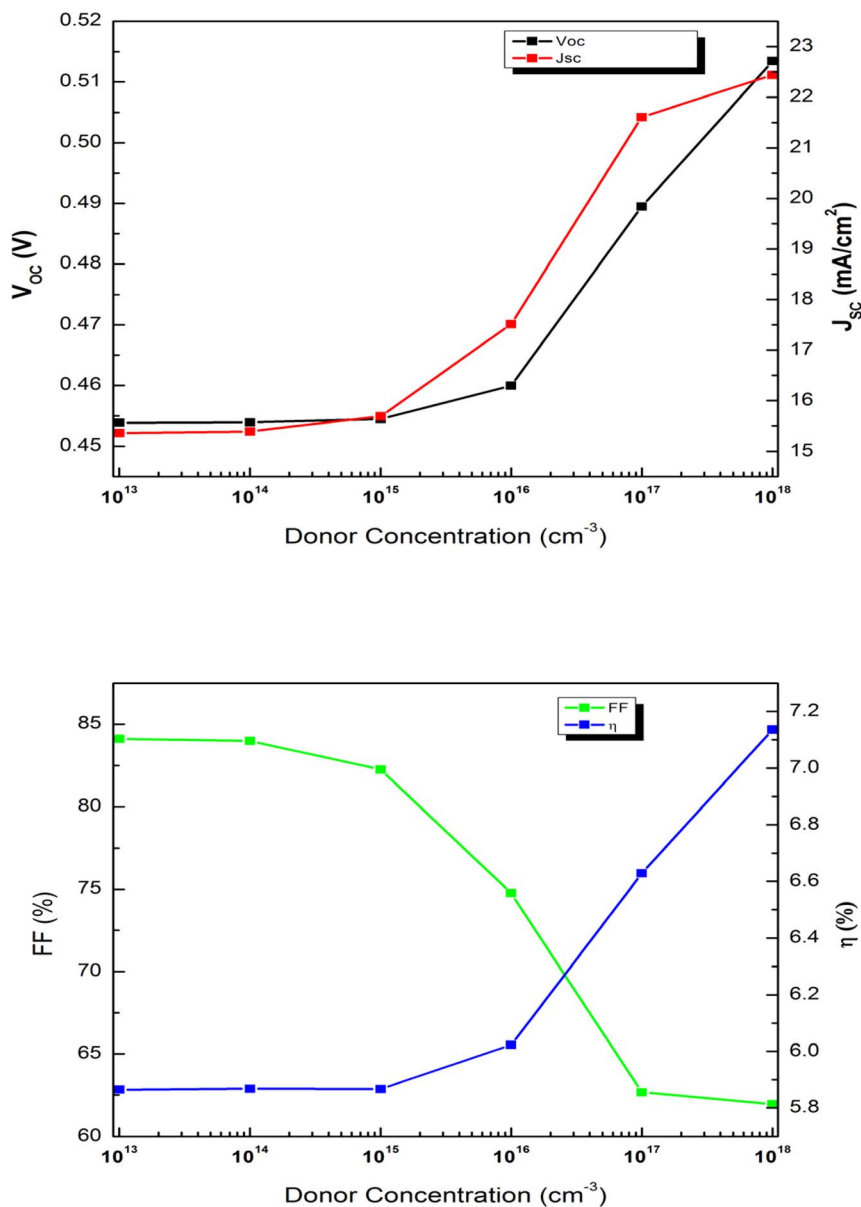


Fig. 8 Photovoltaic output as a function of SnS<sub>2</sub> buffer layer donor concentration.

junction and the SnS<sub>2</sub>//FTO junction rise which augments the separation of the photo-generated charges and efficiency with rise in buffer layer doping concentration.<sup>100</sup> So the buffer layer donor density is optimized at 10<sup>18</sup> cm<sup>-3</sup> which is compatible with published work.<sup>48</sup>

### 3.8 Effect of SnS<sub>2</sub> buffer layer defect density

To examine the influence of SnS<sub>2</sub> buffer layer defect density on photovoltaic characteristics, the defect density is altered from 10<sup>10</sup>–10<sup>18</sup> cm<sup>-3</sup> and photovoltaic output changes obtained are displayed in Fig. 9. All the electrical parameters remain almost constant up to defect density of 10<sup>17</sup> cm<sup>-3</sup>. Thereafter, all parameters start to degrade drastically. FF starts increasing

particularly at 10<sup>17</sup> cm<sup>-3</sup> because of rise in energy barrier height.<sup>93,101</sup> The efficiency decreases from 7.12–5.87% as defect density is increased from 10<sup>17</sup>–10<sup>18</sup> cm<sup>-3</sup>. The enhanced defect density reduces the carriers' diffusion length and life time and as a result, efficiency decreases as photo-generated carriers find it hard to travel.<sup>102</sup> So buffer layer defect density of 10<sup>15</sup> cm<sup>-3</sup> is chosen as optimum value which matches with previous work.<sup>12</sup>

### 3.9 Effect of FTO window layer thickness

The influence of FTO window layer thickness on solar cell output is also simulated. The thickness is altered from 0.1–0.6 μm. Fig. 10 displays the simulation outcomes obtained. It is observed that both V<sub>OC</sub> and J<sub>SC</sub> decrease very slightly and FF



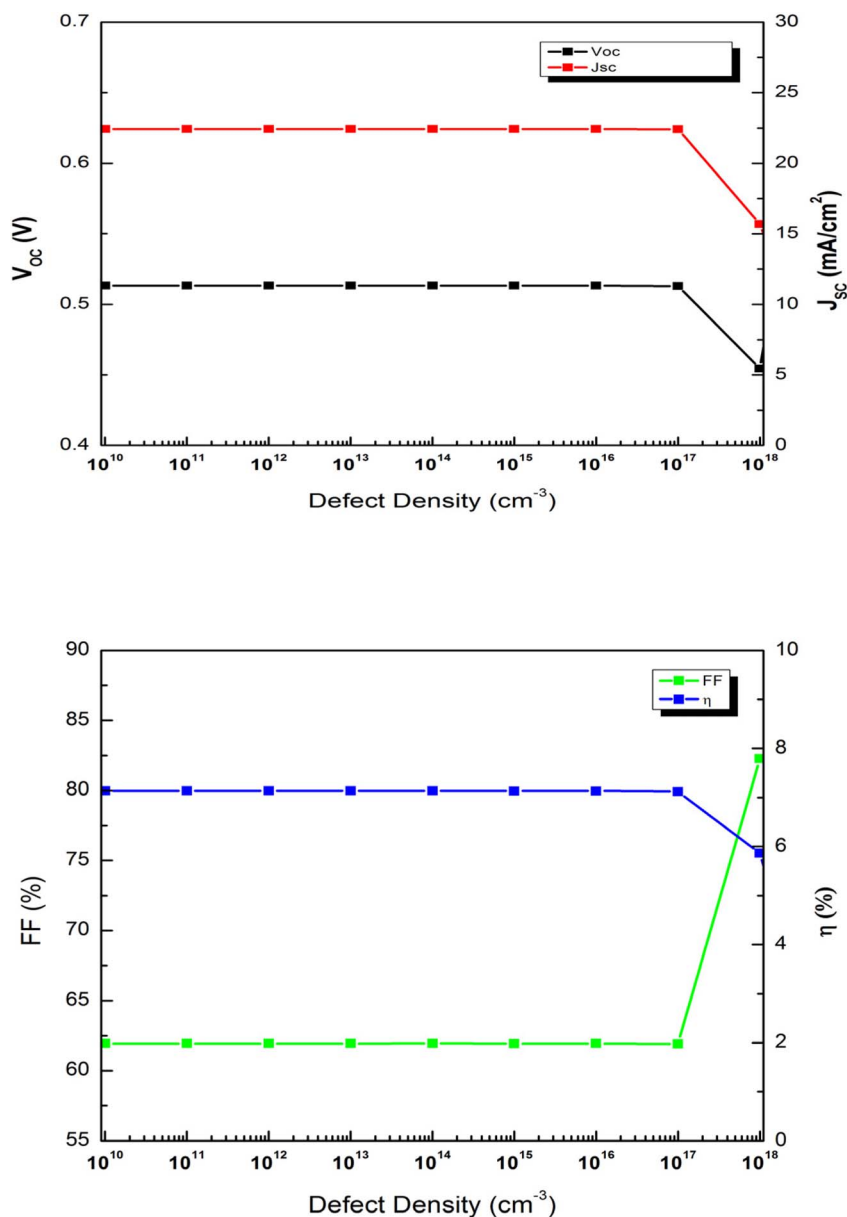


Fig. 9 Effect of SnS<sub>2</sub> buffer layer defect density on photovoltaic output.

remains almost constant as window layer thickness is enhanced within 0.1–0.6  $\mu\text{m}$ . The efficiency decreases from 7.16–7.13% as window layer thickness is varied from 0.1–0.6  $\mu\text{m}$ . As FTO layer thickness rises, the absorption of a large part of the light which incidents in the FTO layer declines transmission, which creates an optical loss and as a result degrades efficiency in the solar cell.<sup>103</sup> So the optimal window layer thickness chosen is 0.1  $\mu\text{m}$ .

### 3.10 Influence of FTO window layer doping concentration

The effect of the FTO window layer donor concentration is examined and simulation results are outlined in Fig. 11. The FTO window layer doping concentration is tuned from  $10^{17}$ –

$10^{20} \text{ cm}^{-3}$ .  $V_{\text{OC}}$  remains constant and both FF and  $J_{\text{SC}}$  increase with increase in window layer donor concentration in considered range. Efficiency increases very slightly from 7.16–7.21% as window layer donor concentration is increased from  $10^{17}$ – $10^{20} \text{ cm}^{-3}$ . It is concluded that the FTO layer doping density has insignificant effect on the performance of the proposed Sb<sub>2</sub>Se<sub>3</sub> based solar cell when compared to the effect of the absorber and buffer layer. The photo-generated carriers may be collected by electrodes efficiently with rise of FTO layer donor density and thus increases efficiency.<sup>104</sup> The optimal window layer donor density chosen is  $10^{20} \text{ cm}^{-3}$  which is compatible with research work.<sup>105</sup>

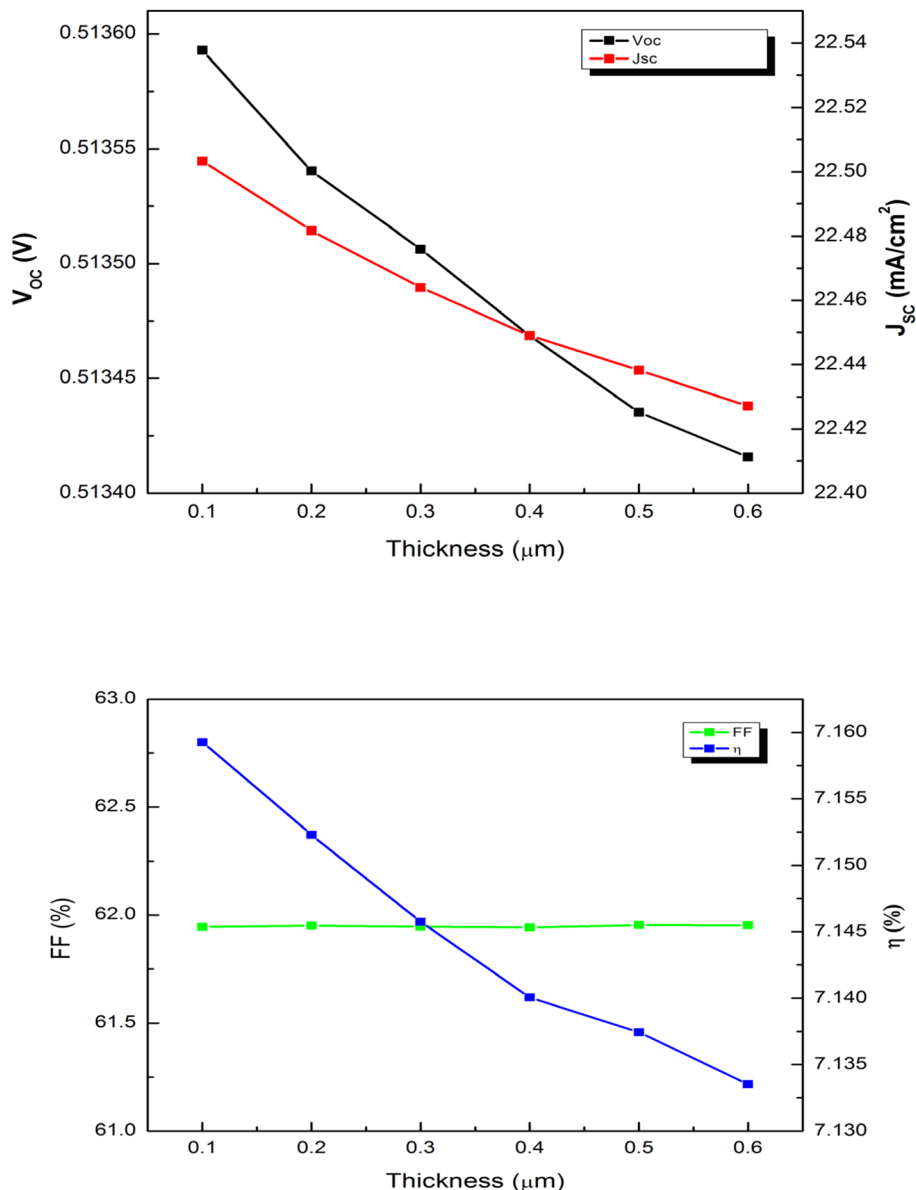


Fig. 10 Impact of FTO window layer thickness on cell output parameters.

### 3.11 Effect of $Sb_2Se_3/SnS_2$ interface defect density

Metallurgical discontinuities, lattice mismatch and symmetry breaking at the interfaces result in interface defects. Interface with low lattice mismatch results in low both interfacial defects and recombination rate and enhances performance parameters. The  $Sb_2Se_3/SnS_2$  interface defect density is altered from  $10^7$   $cm^{-2}$  to  $10^{18}$   $cm^{-2}$  to investigate its impact on device output. Simulation findings are depicted in Fig. 12. It is observed that all performance parameters decrease significantly as interface defect density is increased from  $10^7$   $cm^{-2}$  to  $10^{10}$   $cm^{-2}$ . Afterwards, all performance parameters remain nearly constant. The  $V_{OC}$ ,  $J_{SC}$ , FF and efficiency decreases from 0.52 V to 0.5135 V,

24.19  $mA\ cm^{-2}$  to 22.52  $mA\ cm^{-2}$ , 63.3–62.36% and 7.96–7.21% respectively as interface defect density is increased from  $10^7$ – $10^{18}$   $cm^{-2}$ . Enhanced recombination centers at the  $Sb_2Se_3/SnS_2$  interface due to increase in electron trap centers at high density of  $Sb_2Se_3/SnS_2$  interface defects are responsible for the degradation of performance parameters.<sup>106</sup> The optimal  $Sb_2Se_3/SnS_2$  interface defect density selected is  $10^{10}$   $cm^{-2}$  which is in good agreement with earlier research works.<sup>107,108</sup>

### 3.12 Effect of $Sb_2Se_3$ absorber layer capture cross section

The influence of the  $Sb_2Se_3$  absorber layer capture cross section is investigated by altering the  $Sb_2Se_3$  absorber layer electron and



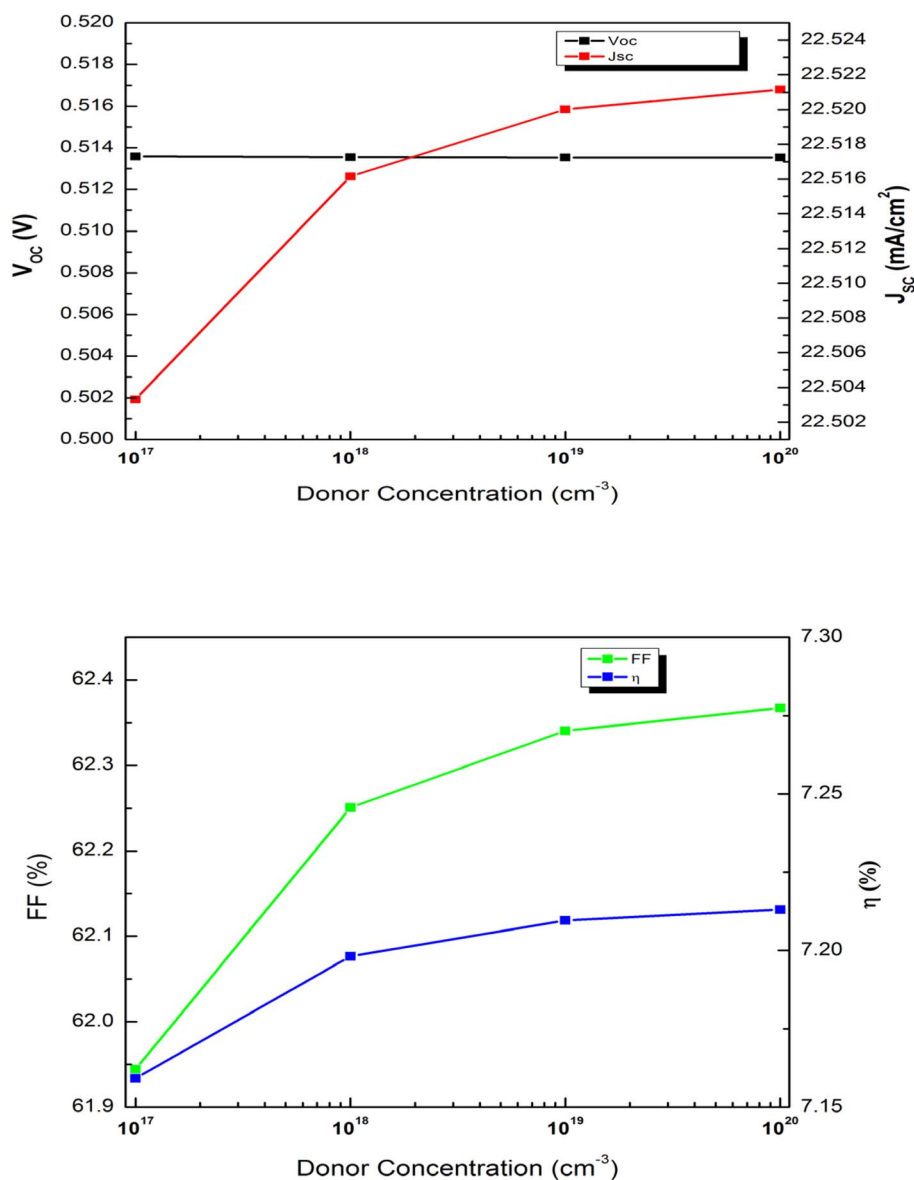


Fig. 11 Impact of FTO window layer donor density on device performance.

hole capture cross section from  $10^{-19}$ – $10^{-9}$  cm<sup>-2</sup>. Simulation results are displayed in Fig. 13. It is observed that both  $V_{OC}$  and  $J_{SC}$  remain almost constant as capture cross section is enhanced from  $10^{-19}$ – $10^{-12}$  cm<sup>-2</sup>. Then both decrease as capture cross section is increased in considered range. Both FF and  $\eta$  remain unaltered as capture cross section is enhanced from  $10^{-19}$ – $10^{-13}$  cm<sup>-2</sup>. Afterwards, both decline as capture cross section is increased in considered range. Efficiency decreases from 10.23–1.24% as capture cross section is enhanced from  $10^{-19}$ – $10^{-9}$  cm<sup>-2</sup>. Both carrier diffusion length and lifetime is declined

because of large lattice mismatch and enhancement of recombination rate as capture cross-section of defect is increased which degrades device performance parameters.<sup>109,110</sup> The optimal Sb<sub>2</sub>Se<sub>3</sub> absorber layer capture cross section selected is  $10^{-15}$  cm<sup>-2</sup> which matches with reported earlier work.<sup>12</sup>

### 3.13 The influence of Sb<sub>2</sub>Se<sub>3</sub>/SnS<sub>2</sub> interface capture cross-section

The Sb<sub>2</sub>Se<sub>3</sub>/SnS<sub>2</sub> interface capture cross section of electron and hole is tuned from  $10^{-20}$ – $10^{-8}$  cm<sup>-2</sup> to examine its impact on



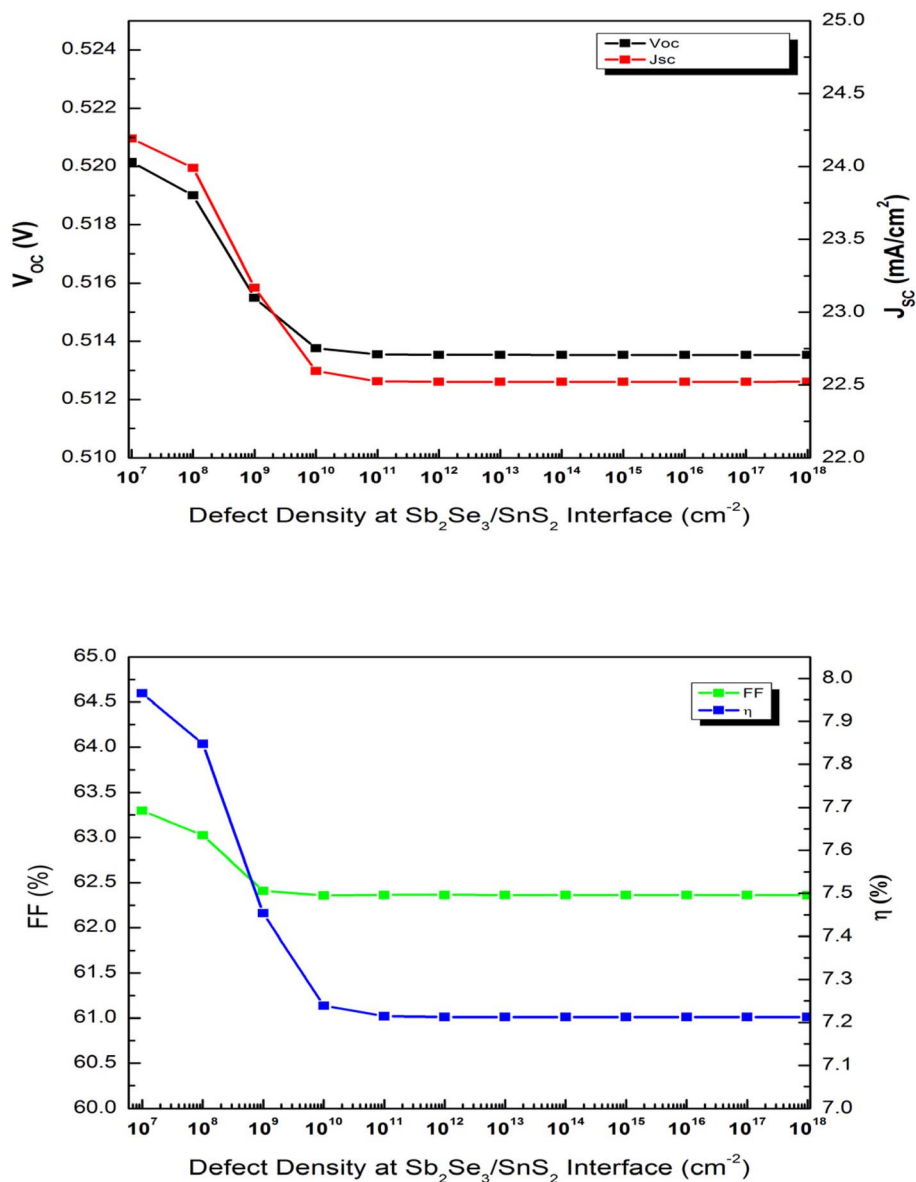


Fig. 12 Influence of Sb<sub>2</sub>Se<sub>3</sub>/SnS<sub>2</sub> interface defect density on cell output.

device output and simulation results are depicted in Fig. 14. It is observed that all performance parameters remain almost constant as capture cross section is enhanced from  $10^{-20}$ – $10^{-13}$  cm<sup>-2</sup>. Then all parameters decline as capture cross section is increased in considered range. Efficiency decreases from 12.31–10.18% as capture cross section is enhanced from  $10^{-20}$  cm<sup>-2</sup> to  $10^{-8}$  cm<sup>-2</sup>. It is evident that interface capture cross-section has less effect on device output compared to absorber capture cross-section of carriers. Enhancement in capture cross-section of electron and hole results in degradation of the Sb<sub>2</sub>Se<sub>3</sub>/SnS<sub>2</sub> interface quality, enhancement in recombination and as

a result, the efficiency declines.<sup>111,112</sup> The optimal Sb<sub>2</sub>Se<sub>3</sub>/SnS<sub>2</sub> interface capture cross section chosen is  $10^{-19}$  cm<sup>-2</sup> which is compatible with research work.<sup>111</sup>

### 3.14 Impact of SnS BSF layer thickness

The BSF layer allows easy transportation of holes and blocks the electrons to the back contact simultaneously. Thus BSF layer has a major role in solar cell performance. The effect of SnS BSF layer thickness on solar cell characteristics is also explored. The thickness is varied from 0.02–0.2 μm. Device performance changes with respect to SnS thickness variation are displayed in



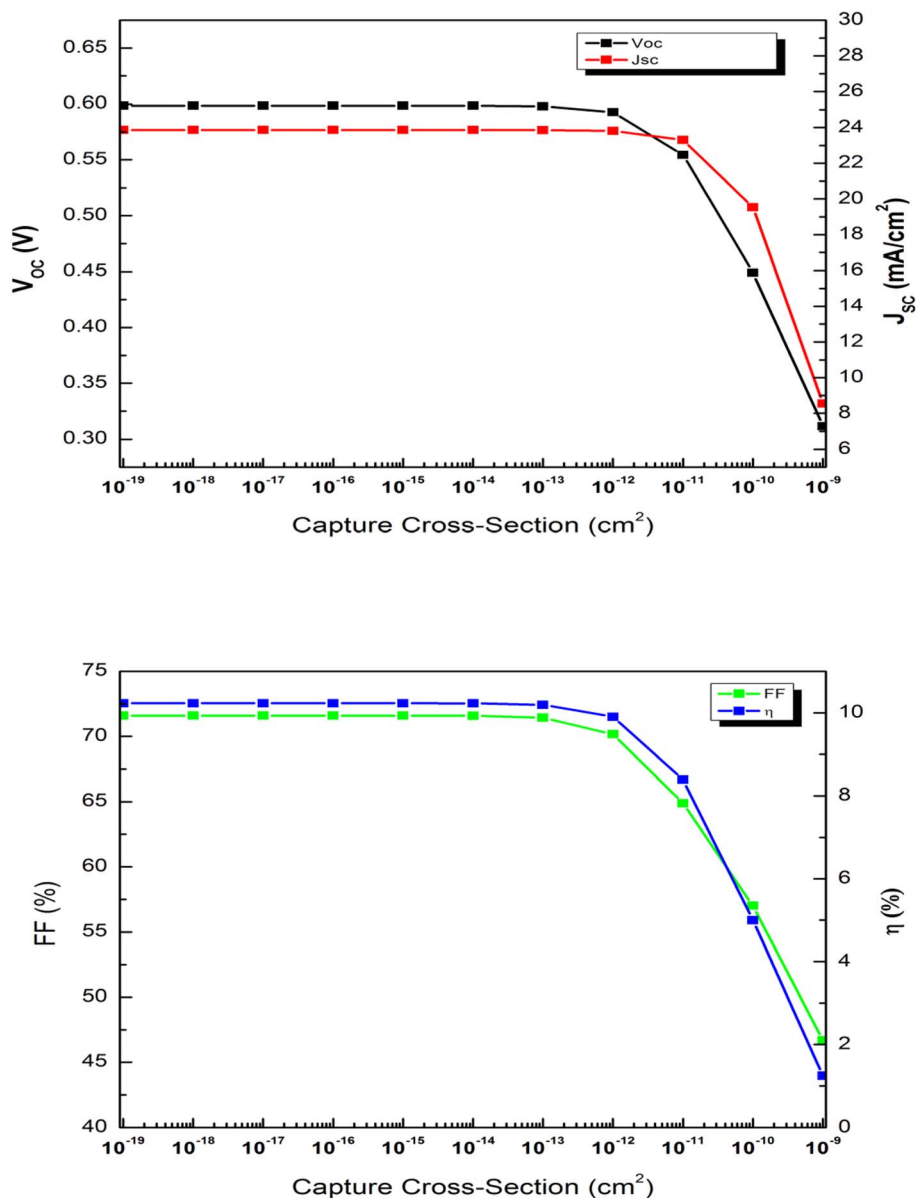


Fig. 13 Effect of  $\text{Sb}_2\text{Se}_3$  absorber layer capture cross-section on device electrical parameters.

Fig. 15. The acceptor concentration and defect density of BSF layer is maintained fixed at  $10^{18} \text{ cm}^{-3}$  and  $10^{14} \text{ cm}^{-3}$  respectively. It is observed that the thickness of SnS shows significant effect on the solar cell performance parameters.  $V_{\text{OC}}$ ,  $J_{\text{SC}}$ , FF and  $\eta$  increases from 0.7 V to 0.83 V,  $26.76 \text{ mA cm}^{-2}$  to  $31.91 \text{ mA cm}^{-2}$ , 80.97–85.96% and 15.12–22.87% as SnS BSF layer thickness is increased from 0.02–0.2  $\mu\text{m}$ . The decrease of recombination rate of carriers with increasing BSF thickness improves both  $V_{\text{OC}}$  and  $J_{\text{SC}}$ .<sup>105</sup> The generation of carriers is increased with the rise in the thickness of BSF layer with the same amount of

incident photon and thus improves efficiency.<sup>91</sup> To minimize production cost and the quantity of material used by the absorber layer, the optimal SnS BSF layer thickness chosen is 0.2  $\mu\text{m}$  which matches with reported study.<sup>98</sup>

### 3.15 Influence of SnS BSF layer acceptor concentration

The effect of the SnS BSF layer acceptor density is examined and simulation outcomes are represented in Fig. 16. The SnS BSF layer doping concentration is tuned from  $10^{15}$ – $10^{20} \text{ cm}^{-3}$ . All electrical parameters except FF enhance with rise in SnS BSF



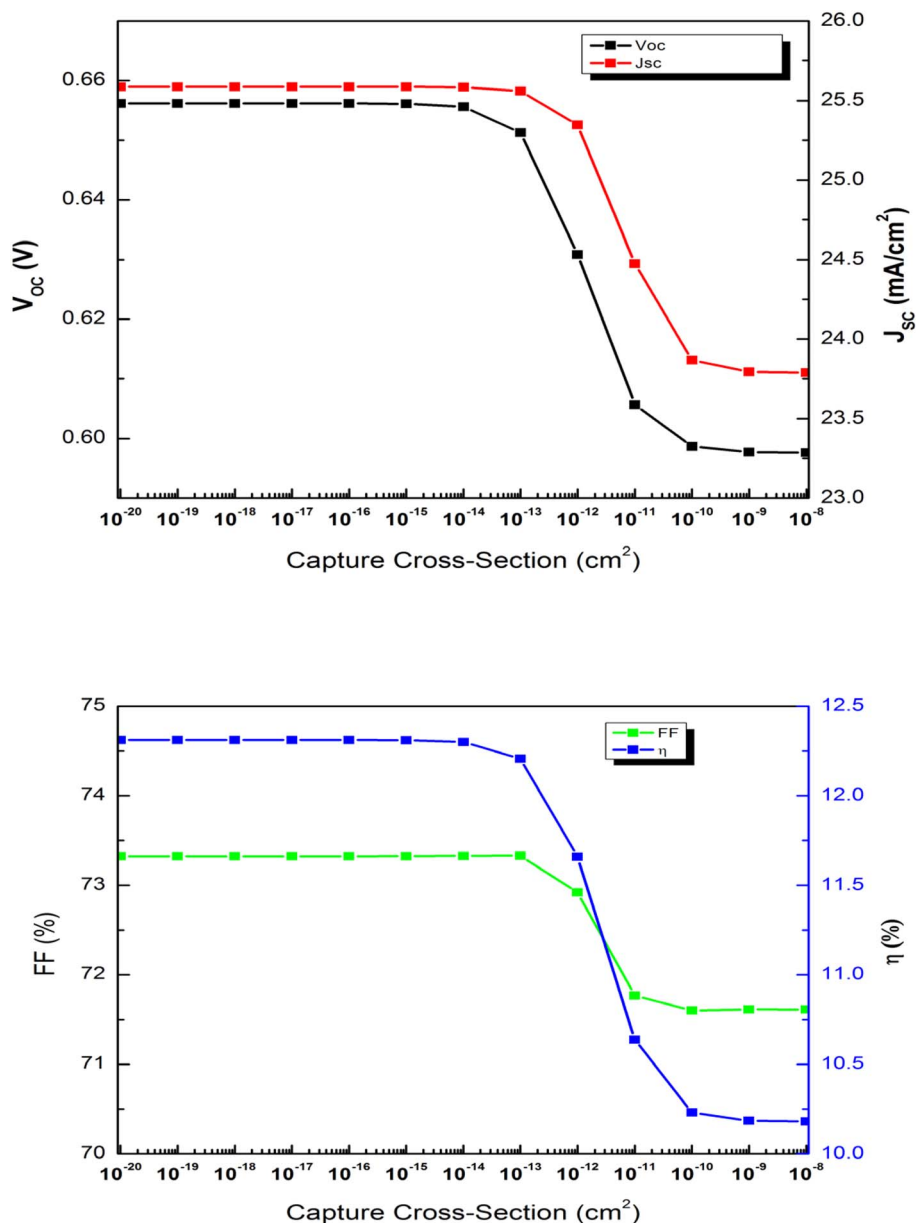


Fig. 14 Solar cell characteristics as a function of  $\text{Sb}_2\text{Se}_3/\text{SnS}_2$  interface capture cross-section.

layer carrier density from  $10^{15}$ – $10^{20} \text{ cm}^{-3}$ . FF increases from 72.65–85.96% as SnS BSF layer acceptor concentration is enhanced from  $10^{15}$ – $10^{18} \text{ cm}^{-3}$  due to decrease in series resistance. Afterwards, FF decline due to increase of recombination at high doping.  $V_{oc}$ ,  $J_{sc}$  and efficiency increases from 0.66 V to 0.94 V,  $26.6 \text{ mA cm}^{-2}$  to  $31.98 \text{ mA cm}^{-2}$  and 12.74–24.86% as doping density of BSF layer is increased from  $10^{15}$ – $10^{20} \text{ cm}^{-3}$ . The large potential created at the SnS/ $\text{Sb}_2\text{Se}_3$  interface reduces recombination rate of carriers at high carrier density of BSF layer. Ohmic contact is created with the back contact due to

closeness of BSF Fermi level with the valence band (VB) at high BSF doping density which supports easy transportation of holes towards back electrode and enhances device performance.<sup>113</sup> The optimal BSF layer acceptor density chosen is  $10^{20} \text{ cm}^{-3}$ . The result is within range of earlier simulation studies.<sup>37,114</sup>

### 3.16 Effect of SnS BSF layer defect density

The SnS BSF layer defect density is varied from  $10^{10}$ – $10^{20} \text{ cm}^{-3}$  to examine its impact on device electrical parameters and simulation outcomes are displayed in Fig. 17. The efficiency is



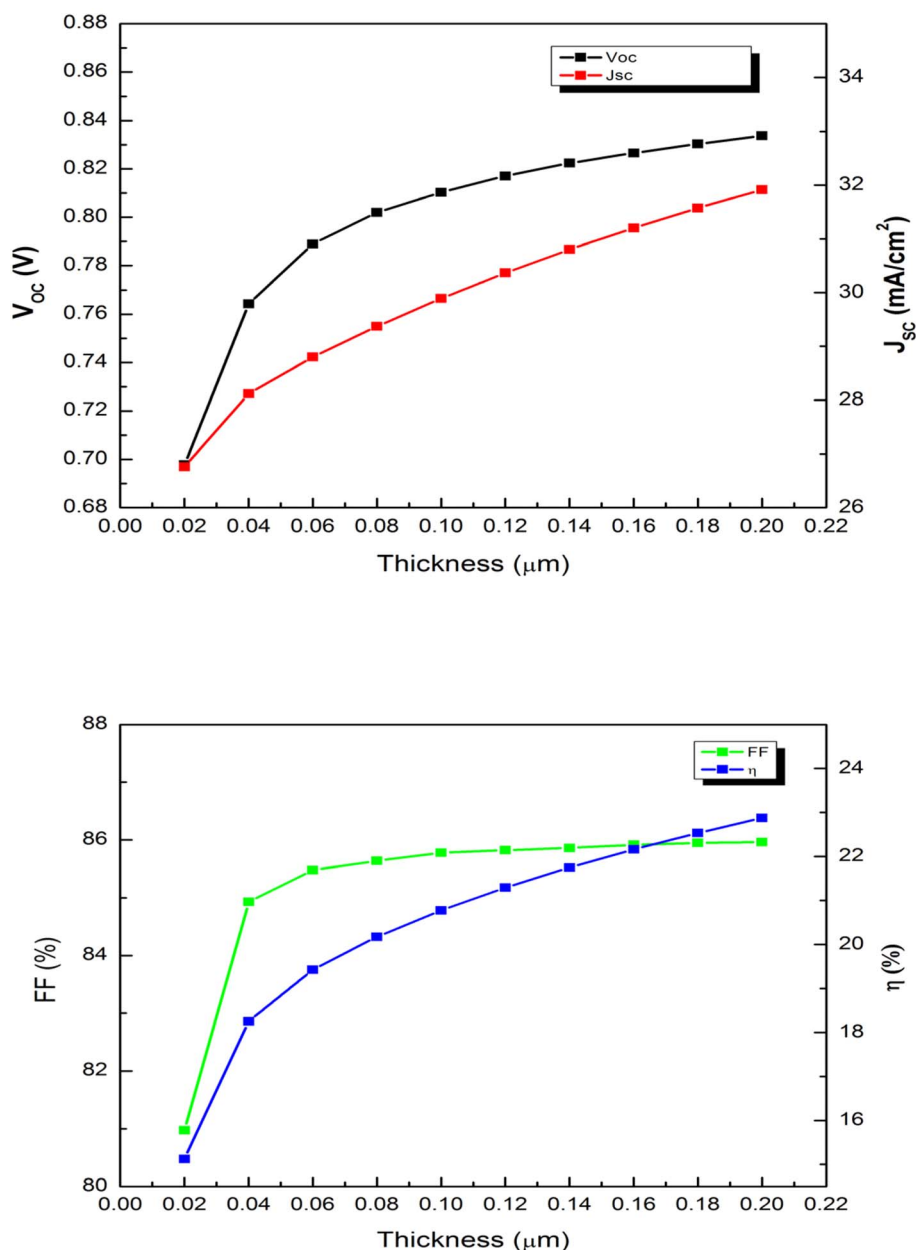


Fig. 15 Effect of SnS BSF layer thickness on device characteristics.

nearly fixed till defect density of  $10^{17} \text{ cm}^{-3}$ . Afterwards, efficiency starts to degrade. The efficiency declines from 24.86–12.79% as defect density is enhanced from  $10^{10}$ – $10^{20} \text{ cm}^{-3}$  due to increase in recombination. The sudden rise in FF from defect density  $10^{17}$ – $10^{19} \text{ cm}^{-3}$  is due to increase in energy barrier height.<sup>93,101</sup> The optimal BSF layer defect density selected is  $10^{14} \text{ cm}^{-3}$  which matches with earlier study.<sup>114</sup>

### 3.17 Impact of back contact work function

The back contact work function majorly impacts the efficiency of the solar cell. A high work function back contact is needed for

a proper ohmic contact at the absorber or BSF/back contact interface. To explore the influence of back contact on photovoltaic output, back contact work function is tuned from 4.5–5.4 eV and simulation outcomes obtained are represented in Fig. 18.  $J_{SC}$  increases by a small margin as work function is enhanced within 4.5–5.4 eV. Both  $V_{OC}$  and FF enhance prior to work function of 5 eV and thereafter stay almost saturated. The combined increase of  $V_{OC}$  and FF enhances the efficiency till work function of 5 eV and then remain saturated. With rise in work function of the back electrode, the carriers' barrier height at the back surface decreases which enhances device



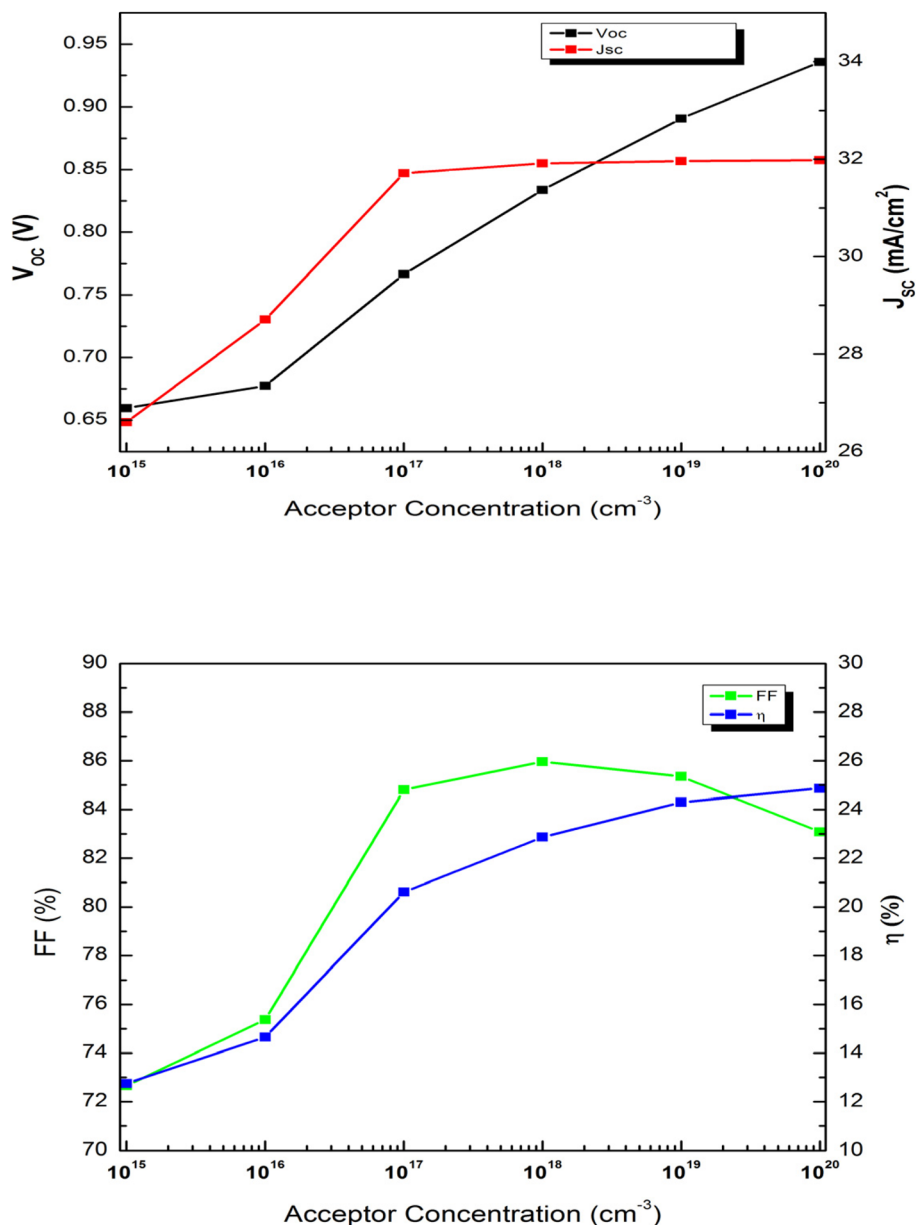


Fig. 16 Impact of SnS BSF layer acceptor density on photovoltaic output.

performance.<sup>14</sup> So for maximum efficiency of proposed solar cell, back electrode work function is required to be larger or equal to 5 eV.

### 3.18 Impact of temperature

Long-term stability under ambient air condition is a major requirement for the application of photovoltaic device. The influence of the working temperature on solar cell is investigated in a range of 300–400 K and the simulation outcomes are depicted in Fig. 19.  $J_{sc}$  increases slightly due to reduction of the bandgap of the absorber which rises the generation of carrier in solar cell as temperature is increased in considered range.<sup>115</sup>

The rise of temperature makes thermally generated electrons unstable due to vibration and recombine with the holes before being collected at the electrodes, reducing  $V_{OC}$  linearly. Moreover, the rise in temperature impacts the carrier properties such as mobility and carrier density and as a result, declines the FF of device.<sup>116</sup> The combined decrease in  $V_{OC}$  and FF declines efficiency from 24.86–20.37% as temperature is enhanced from 300–400 K.

### 3.19 Influence of parasitic resistance

Series resistance ( $R_s$ ) and shunt resistance ( $R_{sh}$ ) have a vital effect on photovoltaic output. The solar cell performs best at



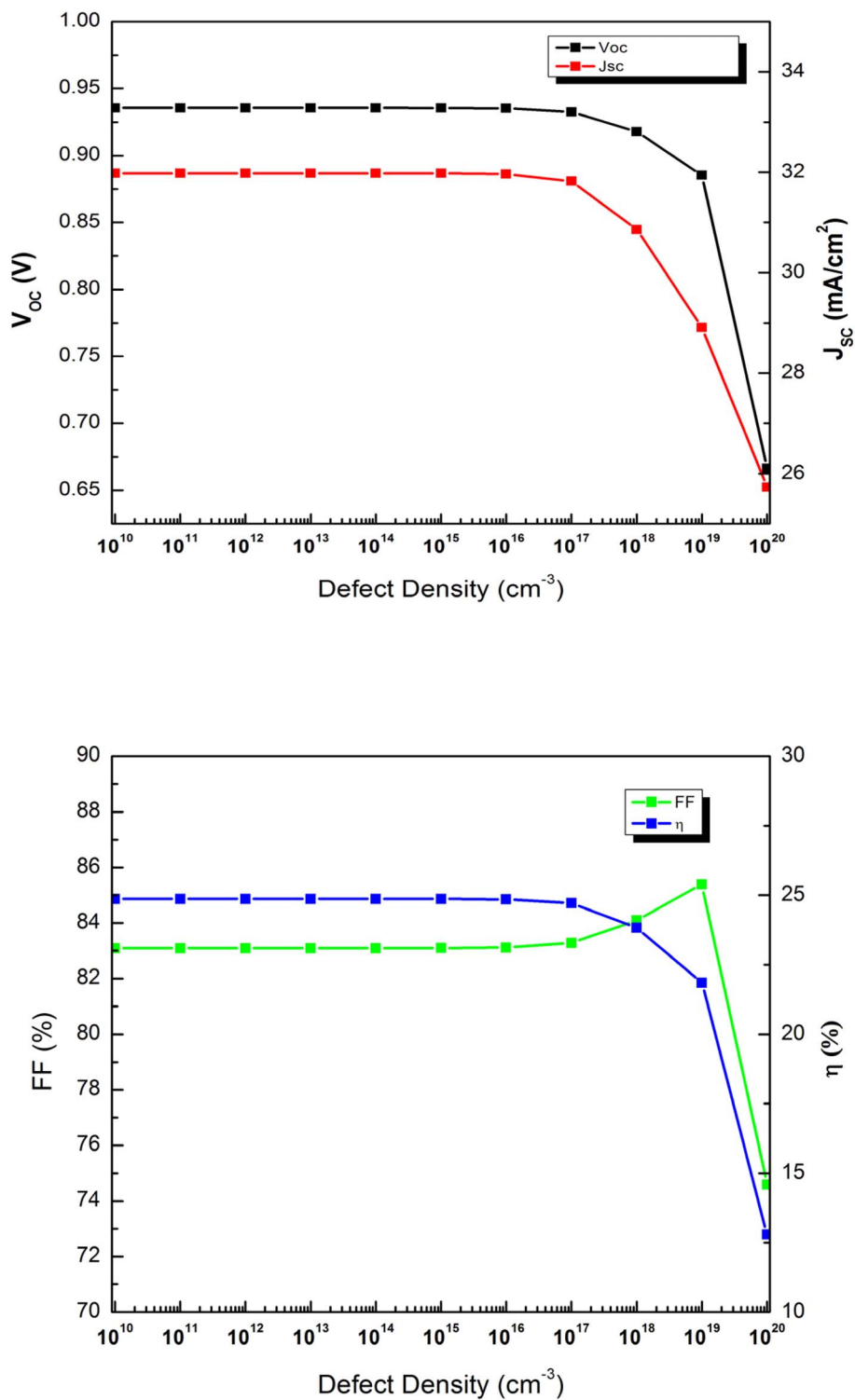


Fig. 17 Influence of SnS BSF layer defect density on cell output parameters.



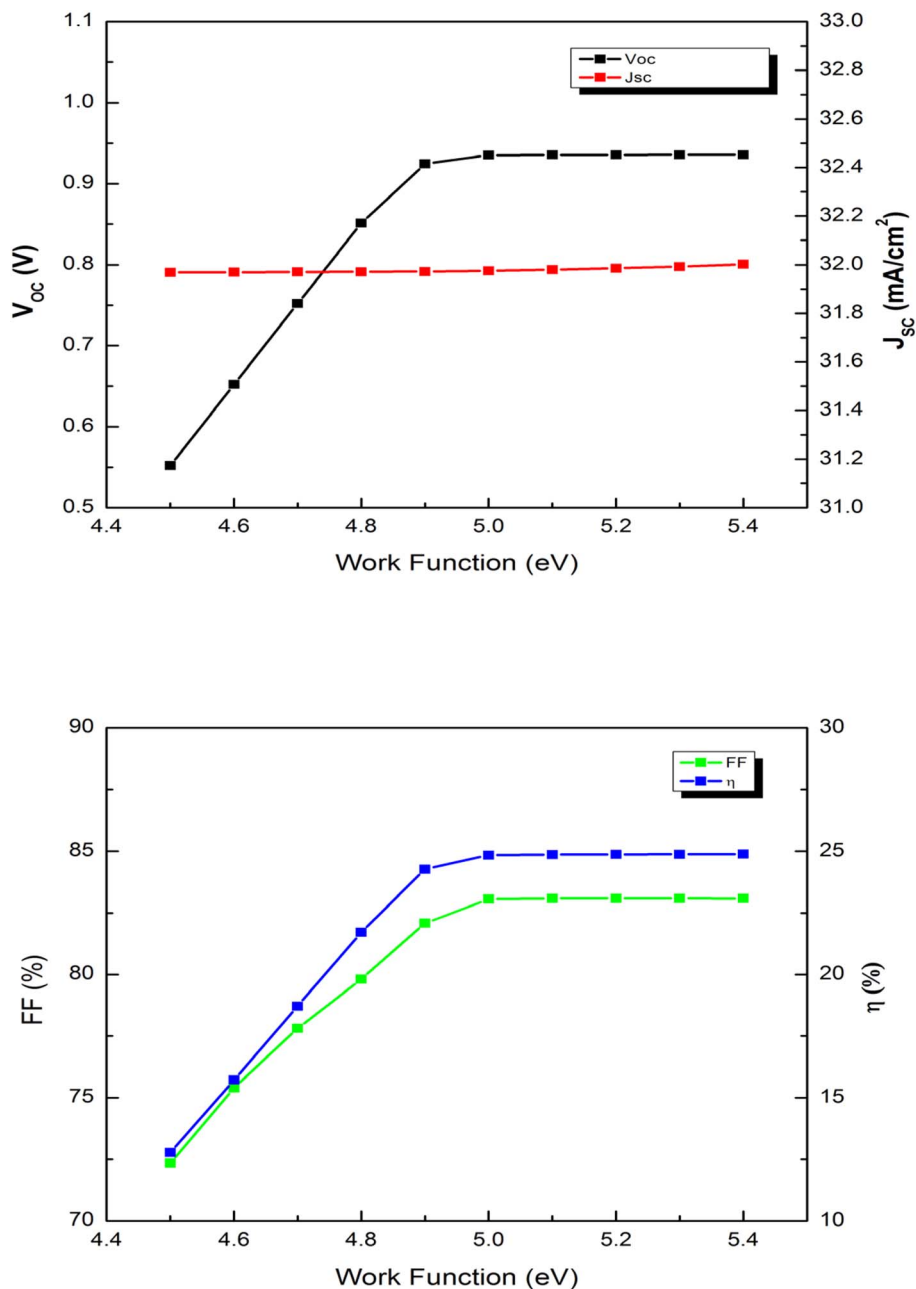


Fig. 18 Impact of back contact work function on device performance with BSF layer.

maximum  $R_{sh}$  and minimum  $R_s$  values.  $R_s$  is the sum of resistance between different layers of solar cells and at the back and front contacts.<sup>117</sup> When the current created by sunlight flows through the various channels produced by small  $R_{sh}$ , efficiency degrades.<sup>14</sup>

The  $Sb_2Se_3$  solar cell performance parameters with SnS BSF layer is investigated by varying the  $R_s$  from 0 to 8  $\Omega\text{ cm}^2$ . The obtained results are shown in Fig. 20. It is observed that  $V_{oc}$  remains constant and  $J_{sc}$  decreases slightly with rise of series

resistance.  $J_{sc}$  decreases because of rise in internal resistance which impedes the transport of carriers to the contacts.<sup>118</sup> FF decreases significantly from 83.09–59.1% with increase of series resistance in considered range. As a result, efficiency decreases from 24.86–17.68% for optimized FTO/SnS<sub>2</sub>/Sb<sub>2</sub>Se<sub>3</sub>/SnS/Au solar cell as  $R_s$  is increased from 0 to 8  $\Omega\text{ cm}^2$ .  $R_s$  should be kept as low as possible to achieve high efficiency.

The  $R_{sh}$  is changed from 200  $\Omega\text{ cm}^2$  to 1600  $\Omega\text{ cm}^2$  to investigate its effect on the cell output with SnS BSF layer and



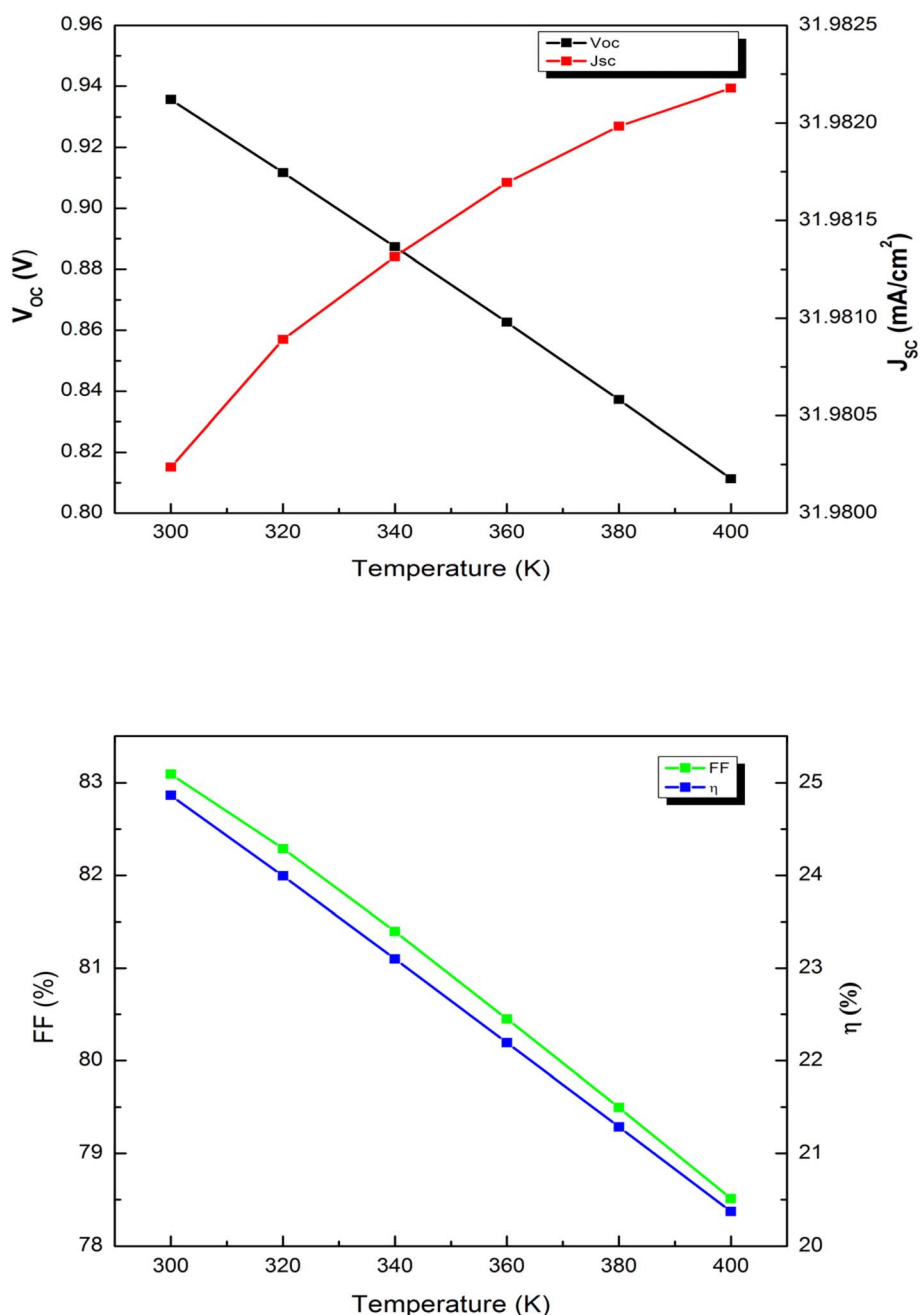


Fig. 19 Solar cell output variation with changes in temperature with BSF layer.

findings are shown in Fig. 21.  $J_{SC}$  is found to be unaltered,  $V_{OC}$  increases slightly and FF rises significantly with increase of shunt resistance in considered range. Efficiency rises from 21.6–24.45% as shunt resistance is increased from 200–1600  $\Omega$   $cm^2$  for proposed  $Sb_2Se_3$  solar cell with SnS BSF layer mainly due to rise of FF. FF increases with increase in  $R_{Sh}$  because of

low recombination rates.<sup>119</sup> It is observed that both FF and efficiency rise with increase in the  $R_{Sh}$  till 1200  $\Omega$   $cm^2$  and almost saturate on further increase in  $R_{Sh}$ . As a result,  $R_{Sh}$  should be high to achieve high efficiency.

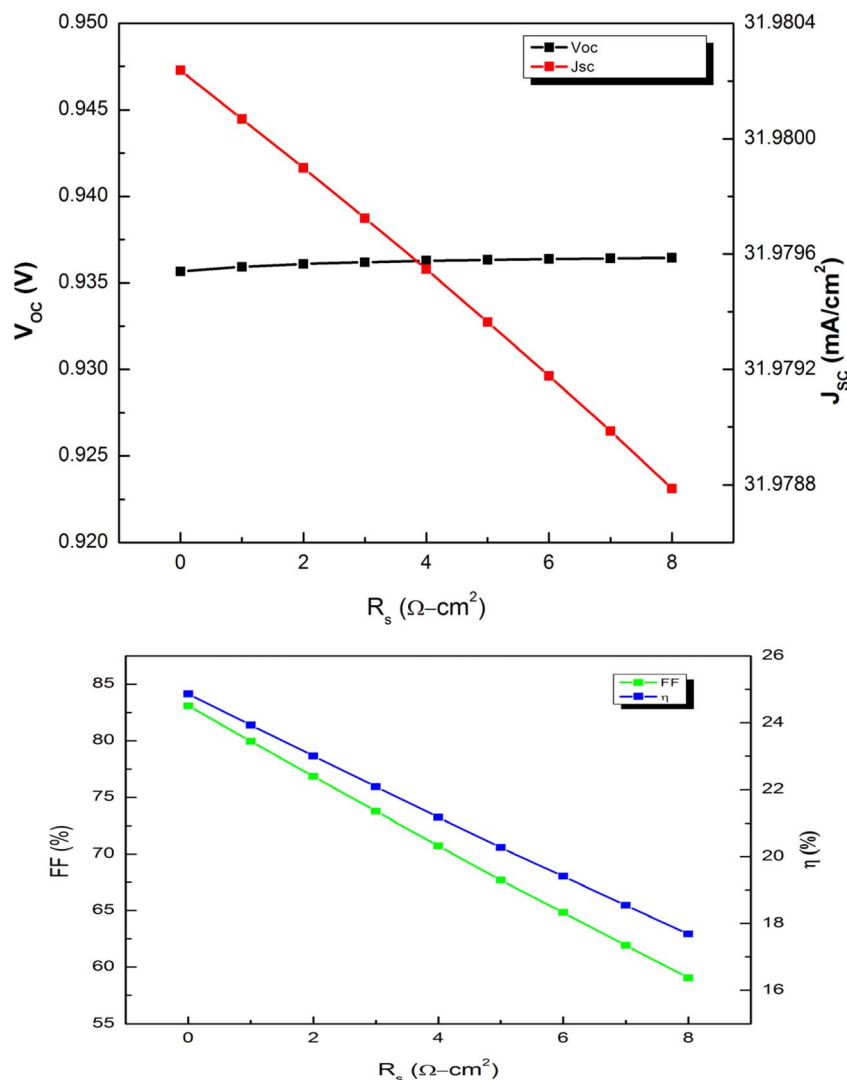


Fig. 20 Effect of series resistance ( $R_s$ ) on cell output parameters with BSF layer.

### 3.20 Overall cell performance

The influence of inserting highly doped p-type SnS BSF layer of  $\text{Sb}_2\text{Se}_3$  based solar cell on the current density–voltage ( $J$ – $V$ ) is depicted in Fig. 22. The electrical parameters of  $\text{Sb}_2\text{Se}_3$  based solar cell without and with SnS BSF layer are summarized in Table 5. The optimum parameters of different layers of FTO/ $\text{SnS}_2$ / $\text{Sb}_2\text{Se}_3$ /SnS/Au solar cell are illustrated in Table 6. The optimized FTO/ $\text{SnS}_2$ / $\text{Sb}_2\text{Se}_3$ /Au solar cell structure obtains  $V_{OC}$ ,  $J_{SC}$ , FF and  $\eta$  of 0.66 V, 25.59  $\text{mA cm}^{-2}$ , 73.33% and 12.31% respectively. The insertion of SnS BSF layer enhances  $V_{OC}$ ,  $J_{SC}$ , FF and  $\eta$  to 0.94 V, 31.98  $\text{mA cm}^{-2}$ , 83.09% and 24.86% respectively. It is noticed that all electrical parameters are enhanced due to addition of SnS BSF layer. The creation of large built-in potential at the  $\text{Sb}_2\text{Se}_3$ /SnS interface rises the value of

$V_{OC}$ .<sup>120</sup> The efficient separation and collection of carriers due to the addition of BSF layer enhances the value of  $J_{SC}$ .<sup>121</sup> The improvement of FF is due to rise in the maximum power produced by FTO/ $\text{SnS}_2$ / $\text{Sb}_2\text{Se}_3$ /SnS/Au solar cell structure due to reduction of recombination rate at back surface due to the insertion of SnS BSF layer.<sup>122</sup> The efficiency has significantly enhanced due to the insertion of SnS BSF layer because of combined increment of  $V_{OC}$ ,  $J_{SC}$  and FF.

The quantum efficiency (QE) curve for  $\text{Sb}_2\text{Se}_3$  based solar cell at initial and with optimization with and without SnS BSF layer is displayed in Fig. 23. The strong back surface electric fields at the SnS/ $\text{Sb}_2\text{Se}_3$  interface due to addition of SnS BSF layer in the simulated cell structure decreases carrier recombination and increases the absorption at the wavelength range from 400 to 1030 nm, which increases the electrical parameters of the



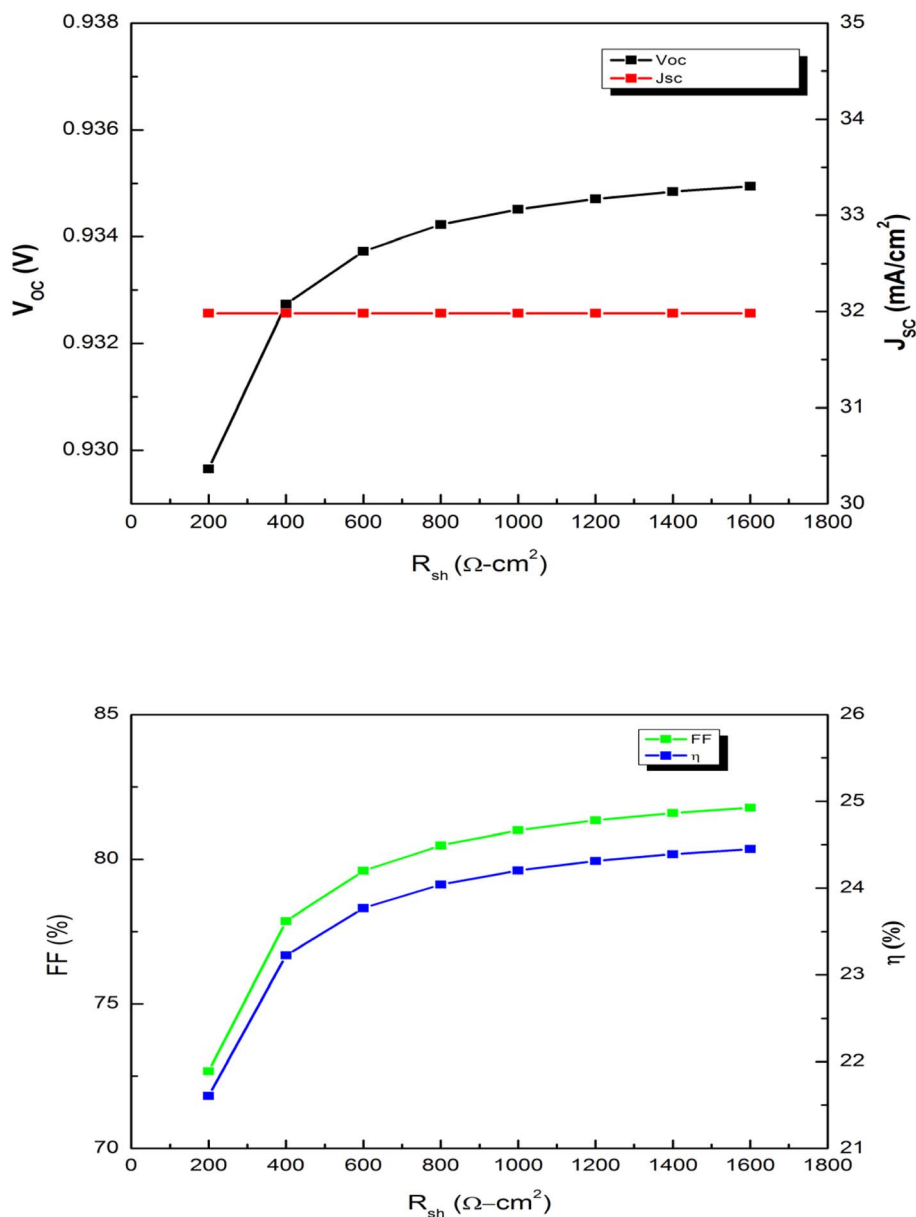


Fig. 21 Impact of shunt resistance ( $R_{sh}$ ) on solar cell characteristics with BSF layer.

designed photovoltaic. This results prove that SnS can be a potential BSF layer for improving the efficiency of  $\text{Sb}_2\text{Se}_3$ -based photovoltaic.

In this research, a promising efficiency of 24.86% was obtained by incorporating SnS as a BSF layer due to  $n\text{-SnS}_2/p\text{-Sb}_2\text{Se}_3/p^+\text{-SnS}$  forming of  $n\text{-p-p}^+$  double heterojunction cell. This double junction cell efficiency improvement can be demonstrated by Tail-States-Assisted (TSA) two-steps photon upconversion process. In this double heterostructure, with the insertion of SnS BSF layer, the sub-bandgap photons may get absorbed notably, specifically in the longer wavelength, which causes an enhancement in solar cell performance. The sub-bandgap photons may be absorbed by the Urbach energy states and these lower energy sub-bandgap photons participate

in tail-state-assisted (TSA) two-steps photon upconversion.<sup>107,123,124</sup> These absorbed photons generate additional electron-hole pairs, resulting in a noticeable improvement in cell photocurrent. A photoactive material such as SnS BSF layer can cause this TSA upconversion effectively when it possesses favorable bandgap, high absorption coefficient and adequate doping concentration.<sup>105,125</sup> Thus, it is believed that this is the main reason of the high-efficiency of 24.86% observed in proposed double heterojunction solar cell. The Urbach energy,  $E_0$ , of the photoactive material determines the resulting increase in photocurrent and the degree of upconversion. The higher Urbach energy remarkably promotes to boosting the quantum efficiency (QE), specifically in the longer wavelength.<sup>5,126</sup>



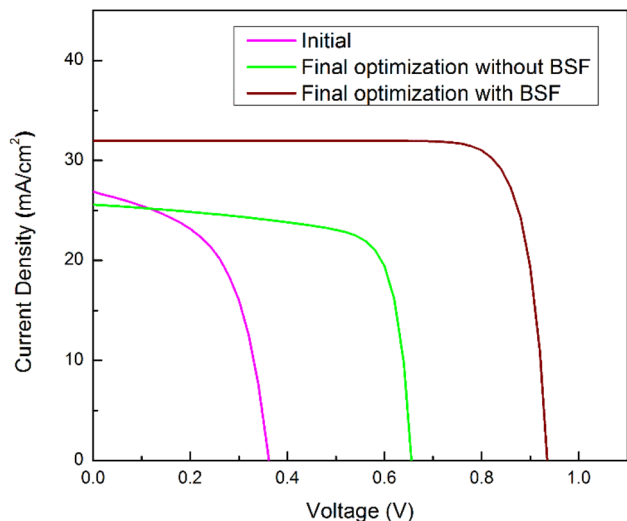


Fig. 22  $J$ - $V$  characteristic curve of  $\text{Sb}_2\text{Se}_3$  based photovoltaic with and without SnS BSF layer.

Table 5 Performance parameters of the proposed FTO/SnS<sub>2</sub>/Sb<sub>2</sub>Se<sub>3</sub>/Au solar cell structure without and with SnS BSF layer

Structure	$V_{OC}$ (V)	$J_{SC}$ (mA cm <sup>-2</sup> )	FF (%)	$\eta$ (%)
FTO/SnS <sub>2</sub> /Sb <sub>2</sub> Se <sub>3</sub> /Au	0.66	25.59	73.33	12.31
FTO/SnS <sub>2</sub> /Sb <sub>2</sub> Se <sub>3</sub> /SnS/Au	0.94	31.98	83.09	24.86

The energy band diagram of the optimized  $\text{Sb}_2\text{Se}_3$ -based solar cell architecture of FTO/SnS<sub>2</sub>/Sb<sub>2</sub>Se<sub>3</sub>/SnS/Au is displayed in Fig. 24. It is noticed that the energy level of conduction and valence band of SnS<sub>2</sub> buffer layer is lower than the  $\text{Sb}_2\text{Se}_3$  absorber layer. As a result, electrons can travel easily to the front contact through the  $\text{Sb}_2\text{Se}_3$ /SnS<sub>2</sub> interface due to small conduction band offset (CBO) of  $-0.05$  eV. On the other hand, the valence band offset (VBO) between the SnS<sub>2</sub> buffer layer and

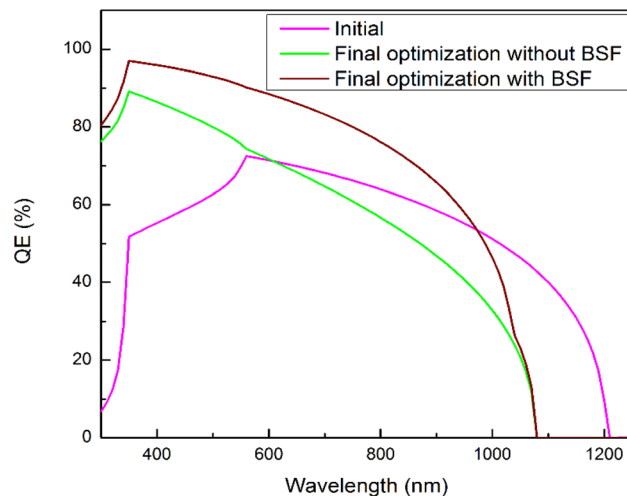


Fig. 23 QE characteristic curve of  $\text{Sb}_2\text{Se}_3$  based photovoltaic with and without SnS BSF layer.

$\text{Sb}_2\text{Se}_3$  absorber layer is large enough to prevent the flow of holes from  $\text{Sb}_2\text{Se}_3$  absorber to front contact. For the SnS BSF layer, the energy level of valence and conduction band is higher than the  $\text{Sb}_2\text{Se}_3$  absorber layer. Moreover, a proper barrier height with a suitable conduction band offset (CBO) at the SnS BSF/ $\text{Sb}_2\text{Se}_3$  absorber junction hinders electrons from travelling from the absorber to the back electrode which in turn reduces recombination process at the back surface.<sup>14,98</sup> On the contrary, the holes can travel from absorber to the back contact easily due to small VBO of 0.1 eV.

### 3.21 Comparative study

Table 7 compares various results from past experimental or theoretical work on  $\text{Sb}_2\text{Se}_3$  based solar cells with various buffer layers without and with BSF layer. In comparison to the previous reported values, enhanced  $\eta$  have been achieved by this simulation study.

Table 6 Optimized parameter values of the FTO/SnS<sub>2</sub>/Sb<sub>2</sub>Se<sub>3</sub>/SnS/Au solar cell

Optimized parameter	Value
$\text{Sb}_2\text{Se}_3$ absorber layer thickness	0.4 $\mu\text{m}$
$\text{Sb}_2\text{Se}_3$ absorber layer acceptor concentration	$10^{16}$ cm <sup>-3</sup>
$\text{Sb}_2\text{Se}_3$ absorber layer defect density	$10^{13}$ cm <sup>-3</sup>
$\text{Sb}_2\text{Se}_3$ absorber layer bandgap	1.15 eV
SnS <sub>2</sub> buffer layer thickness	0.03 $\mu\text{m}$
SnS <sub>2</sub> buffer layer donor concentration	$10^{18}$ cm <sup>-3</sup>
SnS <sub>2</sub> buffer layer defect density	$10^{15}$ cm <sup>-3</sup>
FTO window layer thickness	0.1 $\mu\text{m}$
FTO window layer donor concentration	$10^{20}$ cm <sup>-3</sup>
$\text{Sb}_2\text{Se}_3$ /SnS <sub>2</sub> interface layer defect density	$10^{10}$ cm <sup>-2</sup>
$\text{Sb}_2\text{Se}_3$ absorber layer capture cross-section of electron and hole	$10^{-15}$ cm <sup>-2</sup>
$\text{Sb}_2\text{Se}_3$ /SnS <sub>2</sub> interface capture cross-section of electron and hole	$10^{-19}$ cm <sup>-2</sup>
SnS BSF layer thickness	0.2 $\mu\text{m}$
SnS BSF layer acceptor concentration	$10^{20}$ cm <sup>-3</sup>
SnS BSF layer defect density	$10^{14}$ cm <sup>-3</sup>
Back contact work function	5 eV



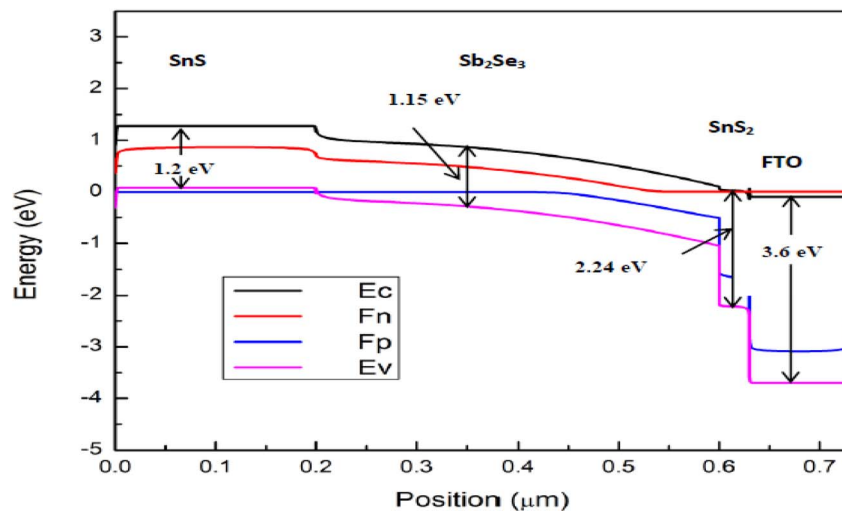


Fig. 24 Energy band diagram of proposed FTO/SnS<sub>2</sub>/Sb<sub>2</sub>Se<sub>3</sub>/SnS/Au solar cell.

Table 7 Comparison of proposed solar cell with other reported Sb<sub>2</sub>Se<sub>3</sub> based solar cells

Structure	Study type	Photovoltaic parameters				References
		V <sub>OC</sub> (V)	J <sub>SC</sub> (mA cm <sup>-2</sup> )	FF (%)	η (%)	
FTO/CdS/Sb <sub>2</sub> Se <sub>3</sub> /CZTA/Au	Experimental	0.421	28.40	57.10	6.84	73
Ag/ITO/ZnO/CdS/Sb <sub>2</sub> Se <sub>3</sub> /Mo/SLG	Experimental	0.454	18.4	50.6	4.22	127
Ag/ITO/CdS/Sb <sub>2</sub> Se <sub>3</sub> /Mo	Experimental	0.343	16.79	35.3	2.1	128
FTO/CdS/Sb <sub>2</sub> Se <sub>3</sub> /Spiro-OMeTAD/Au	Experimental	0.360	29.00	51.50	5.40	55
ITO/CdS/Sb <sub>2</sub> Se <sub>3</sub> /Au	Experimental	0.379	27.93	55.6	5.91	129
AZO/i-ZnO/CdS/TiO <sub>2</sub> /Sb <sub>2</sub> Se <sub>3</sub> /Mo	Experimental	0.4	32.58	70.30	9.20	19
ITO/CdS/Sb <sub>2</sub> Se <sub>3</sub> /CuSCN/Au	Experimental	0.413	30.51	58.99	7.5	130
ITO/CdS/Sb <sub>2</sub> Se <sub>3</sub> /Au	Experimental	0.420	29.90	60.40	7.60	26
Metal contact/ZnO:Al/i-ZnO/CdS/Sb <sub>2</sub> Se <sub>3</sub> /Mo	Simulation	0.56	31.79	70.81	12.62	33
ZnO:Al/ZnO/CdS/TiO <sub>2</sub> /Sb <sub>2</sub> Se <sub>3</sub> /MoS <sub>2</sub> /Mo	Simulation	0.4	32.56	70.3	9.17	131
FTO/Zn(Sn,O)/Sb <sub>2</sub> Se <sub>3</sub> /CZTSe/Au	Simulation	0.66	34.66	81.18	18.50	132
Ag/phenyl-C61-butyric acid methyl ester (PCBM)/Sb <sub>2</sub> Se <sub>3</sub> /HTL/ITO	Simulation	0.858	34.18	84.04	24.66	133
Ag/ZnSe/Sb <sub>2</sub> Se <sub>3</sub> /Mo	Simulation	0.85	34	83.6	24.0	17
Al/ITO/CdS/Sb <sub>2</sub> Se <sub>3</sub> /CuS/Ni	Simulation	0.761	37.59	80.97	23.16	12
FTO/SnS <sub>2</sub> /Sb <sub>2</sub> Se <sub>3</sub> /Au	Simulation	0.66	25.59	73.33	12.31	This work
FTO/SnS <sub>2</sub> /Sb <sub>2</sub> Se <sub>3</sub> /SnS/Au	Simulation	0.94	31.98	83.09	24.86	This work

## 4. Conclusions

The electrical parameters of Sb<sub>2</sub>Se<sub>3</sub>-based thin film solar cell with and without SnS BSF layer have been compared in this simulation work using SCAPS-1D. First of all, experimental result is reproduced for FTO/CdS/Sb<sub>2</sub>Se<sub>3</sub>/Au solar cell structure to validate the numerical model and carry out analysis. Next, non-toxic SnS<sub>2</sub> has been used as a buffer layer instead of the hazardous cadmium sulfide (CdS) for the proposed solar cell which results in enhanced efficiency. Afterwards, to maximize efficiency different parameters such as thickness, doping concentration, bandgap, capture cross section and defect density that effect the electrical output is optimized. The optimal thickness for the Sb<sub>2</sub>Se<sub>3</sub> absorber layer, SnS<sub>2</sub> buffer layer and FTO window layer have been chosen to be of 0.4 μm, 0.03 μm and 0.1 μm respectively. The doping density have been

optimized to be of 10<sup>16</sup> cm<sup>-3</sup>, 10<sup>18</sup> cm<sup>-3</sup> and 10<sup>20</sup> cm<sup>-3</sup> respectively. The defect density in the Sb<sub>2</sub>Se<sub>3</sub> absorber layer, SnS<sub>2</sub> buffer layer and the interface defect at Sb<sub>2</sub>Se<sub>3</sub>/SnS<sub>2</sub> interface have been selected to be of 10<sup>13</sup> cm<sup>-3</sup>, 10<sup>15</sup> cm<sup>-3</sup> and 10<sup>10</sup> cm<sup>-2</sup> respectively for optimal performance. The capture cross-section in the Sb<sub>2</sub>Se<sub>3</sub> absorber layer and at Sb<sub>2</sub>Se<sub>3</sub>/SnS<sub>2</sub> interface have been optimized to be of 10<sup>-15</sup> cm<sup>-2</sup> and 10<sup>-19</sup> cm<sup>-2</sup> respectively. The optimized FTO/SnS<sub>2</sub>/Sb<sub>2</sub>Se<sub>3</sub>/Au solar cell structure provides J<sub>SC</sub> of 25.59 mA cm<sup>-2</sup>, V<sub>OC</sub> of 0.66 V, FF of 73.33% and efficiency of 12.31%. The insertion of SnS BSF layer with thickness of 0.2 μm, carrier density of 10<sup>20</sup> cm<sup>-3</sup> and defect density of 10<sup>14</sup> cm<sup>-3</sup> results in enhanced efficiency of 24.86% including J<sub>SC</sub> of 31.98 mA cm<sup>-2</sup>, V<sub>OC</sub> of 0.94 V and FF of 83.09% for optimized novel FTO/SnS<sub>2</sub>/Sb<sub>2</sub>Se<sub>3</sub>/SnS/Au solar cell structure. The findings of this simulation work provide guidelines



for the production of non-toxic, cost-effective and highly efficient  $\text{Sb}_2\text{Se}_3$ -based solar cell.

## Conflicts of interest

The author declares that there is no conflict of interest regarding the publication of this paper.

## Data availability

The data will be made available on reasonable request.

## Acknowledgements

This research did not receive any specific grant from funding agencies in the public, commercial, or not-for-profit sectors. The author is grateful to Dr Marc Burgelman at University of Ghent, Belgium for allowing to use the SCAPS-1D simulation package.

## References

- 1 S. Saurabh, M. K. Hossain, S. Singh, S. K. Agnihotri and D. P. Samajdar, Optical performance analysis of InP nanostructures for photovoltaic applications, *RSC Adv.*, 2023, **13**, 9878–9891.
- 2 M. R. Islam, M. S. Islam, M. Y. Zamil, N. Ferdous, C. Stamp, J. Park and M. K. Hossain, Two-dimensional BAs/GeC van der waals heterostructures: A widely tunable photocatalyst for water splitting and hydrogen production, *J. Phys. Chem. Solids*, 2023, **176**, 111263.
- 3 M. Shahbaz, A. Siddiqui, M. Siddiqui, Z. Jiao and P. Kautish, Exploring the growth of sustainable energy Technologies: A review, *SUSTAIN*, 2023, **57**, 103157.
- 4 M. H. K. Rubel, S. K. Mitro, M. K. Hossain, K. M. Hossain, M. M. Rahaman, J. Hossain, B. K. Mondal, A. Akter, M. F. Rahman, I. Ahmed and A. K. M. A. Islam, First-principles calculations to investigate physical properties of single-cubic  $(\text{Ba}_{0.82}\text{K}_{0.18})(\text{Bi}_{0.53}\text{Pb}_{0.47})\text{O}_3$  novel perovskite superconductor, *Mater. Today Commun.*, 2022, **33**, 104302.
- 5 J. A. Mahmud, M. F. Rahman, A. Kuddus, M. H. Ali, A. T. M. S. Islam, M. D. Haque, S. R. A. Ahmed, M. Mushtaq and A. B. M. Ismail, Design and analysis of  $\text{SnS}_2/\text{WS}_2/\text{V}_2\text{O}_5$  double-heterojunction toward high performance photovoltaics, *Energy Adv.*, 2023, **2**, 1843–1858.
- 6 A. Laidouci, M. Lamba, V. N. Singh, P. K. Dakua and D. K. Panda, Performance evaluation of  $\text{ZnSnN}_2$  solar cells with Si back surface field using SCAPS-1D: a theoretical study, *Heliyon*, 2023, **9**, e20601.
- 7 M. E. Islam, M. R. Islam, S. Ahmmed, M. K. Hossain and M. F. Rahman, Highly Efficient SnS-Based Inverted Planar Heterojunction Solar Cell with ZnO ETL, *Phys. Scr.*, 2023, **98**, 065501.
- 8 S. Kashyap, J. Madan, M. K. A. Mohammed, M. Khalid Hossain, S. Ponnusamy and R. Pandey, Unlocking the potential of  $\text{MgF}_2$  textured surface in enhancing the efficiency of perovskite solar cells, *Mater. Lett.*, 2023, **339**, 134096.
- 9 S.-C. Yang, T.-Y. Lin, M. Ochoa, H. Lai, R. K. Kothandaraman, F. Fu, A. N. Tiwari and R. Carron, Efficiency boost of bifacial  $\text{Cu}(\text{In,Ga})\text{Se}_2$  thin-film solar cells for flexible and tandem applications with silver-assisted low-temperature process, *Nat. Energy*, 2023, **8**, 40–51.
- 10 N. Shrivastav, S. Kashyap, J. Madan, A. K. Al-Mousoi, M. K. A. Mohammed, M. K. Hossain, R. Pandey and J. Ramanujam, Perovskite-CIGS monolithic tandem solar cells with 29.7% efficiency: A numerical study, *Energy Fuels*, 2023, **37**, 3083–3090.
- 11 M. A. Islam, A. Jawad, N. A. Jahan and M. M. Hossain, Outstanding conversion efficiency of 38.39% from a Perovskite/CIGS tandem PV cell: A synergic optimization through computational modeling, *Heliyon*, 2023, **9**, e20558.
- 12 A. E. Khalfi, M. Ouhadou, I. Rais, F. Essahlaoui, M. F. Rahman, M. Sahal, L. Elmaimouni and A. Benami, A numerical approach to maximizing efficiency in  $\text{Sb}_2\text{Se}_3$  solar cells by using CuS as a hole transport material, *Eur. Phys. J. Plus*, 2023, **138**, 1085.
- 13 M. A. Mughal, R. Engelken and R. Sharma, Progress in indium (III) sulfide ( $\text{In}_2\text{S}_3$ ) buffer layer deposition techniques for CIS, CIGS, and CdTe-based thin film solar cells, *Sol. Energy*, 2015, **120**, 131–146.
- 14 B. Islam, A. Hosen, T. M. Khan, M. F. Rahman, M. H. Rahman, M. S. Islam and S. R. A. Ahmed, Simulating the effect of inserting  $\text{Sb}_2\text{S}_3$  as hole transport layer on SnS-based thin-film solar cells, *J. Electron. Mater.*, 2024, **53**, 4726–4739.
- 15 W. Wang, M. T. Winkler, O. Gunawan, T. Gokmen, T. K. Todorov, Y. Zhu and D. B. Mitzi, Device characteristics of CZTSSe thin-film solar cells with 12.6% efficiency, *Adv. Energy Mater.*, 2014, **4**, 1301465.
- 16 C. Chen, L. Wang, L. Gao, D. Nam, D. Li, K. Li, Y. Zhao, C. Ge, H. Cheong, H. Liu, H. Song and J. Tang, 6.5% certified efficiency  $\text{Sb}_2\text{Se}_3$  solar cells using PbS colloidal quantum dot film as hole-transporting layer, *ACS Energy Lett.*, 2017, **2**, 2125–2132.
- 17 R. Kumari, M. Mamta, R. Kumar, Y. Singh and V. N. Singh, 24% efficient, simple  $\text{ZnSe}/\text{Sb}_2\text{Se}_3$  heterojunction solar cell: An analysis of PV characteristics and defects, *ACS Omega*, 2023, **8**, 1632–1642.
- 18 L. Wang, D.-B. Li, K. Li, C. Chen, H.-X. Deng, L. Gao, Y. Zhao, F. Jiang, L. Li, F. Huang, Y. He, H. Song, G. Niu and J. Tang, Stable 6%-efficient  $\text{Sb}_2\text{Se}_3$  solar cells with a ZnO buffer layer, *Nat. Energy*, 2017, **2**, 17046.
- 19 Z. Li, X. Liang, G. Li, H. Liu, H. Zhang, J. Guo, J. Chen, K. Shen, X. San, W. Yu, R. E. I. Schropp and Y. Mai, 9.2%-efficient core-shell structured antimony selenide nanorod array solar cells, *Nat. Commun.*, 2019, **10**, 125.
- 20 A. T. Ngoupo, S. Ouedraogo, F. Zougmore and J. M. B. Ndjaka, Numerical analysis of ultrathin  $\text{Sb}_2\text{Se}_3$ -based solar cells by SCAPS-1D numerical simulator device, *Chin. J. Phys.*, 2021, **70**, 1–13.



- 21 Y. Lai, Z. Chen, C. Han, L. Jiang, F. Liu, J. Li and Y. Liu, Preparation and characterization of  $\text{Sb}_2\text{Se}_3$  thin films by electrodeposition and annealing treatment, *Appl. Surf. Sci.*, 2012, **261**, 510–514.
- 22 Y. Zhou, L. Wang, S. Chen, S. Qin, X. Liu, J. Chen, D. J. Xue, M. Luo, Y. Cao, Y. Cheng, E. H. Sargent and J. Tang, Thin-film  $\text{Sb}_2\text{Se}_3$  photovoltaics with oriented one-dimensional ribbons and benign grain boundaries, *Nat. Photonics*, 2015, **9**, 409–415.
- 23 S. Messina, M. T. S. Nair and P. K. Nair, Antimony selenide absorber thin films in all-chemically deposited solar cells, *J. Electrochem. Soc.*, 2009, **156**, H327–H332.
- 24 Y.-C. Choi, T.-N. Mandal, W.-S. Yang, Y.-H. Lee, S.-H. Im, J.-H. Noh and S.-I. Seok,  $\text{Sb}_2\text{Se}_3$ -sensitized Inorganic-organic heterojunction solar cells fabricated using a single-source precursor, *Angew. Chem., Int. Ed.*, 2014, **53**, 1329–1333.
- 25 Y. Zhou, M. Leng, Z. Xia, J. Zhong, H. Song, X. Liu, B. Yang, J. Zhang, J. Chen, K. Zhou, J. Han, Y. Cheng and J. Tang, Solution processed antimony selenide heterojunction solar cells, *Adv. Energy Mater.*, 2014, **4**, 1301846.
- 26 X. Wen, C. Chen, S. Lu, K. Li, R. Kondrotas, Y. Zhao, W. Chen, L. Gao, C. Wang, J. Zhang, G. Niu and J. Tang, Vapor transport deposition of antimony selenide thin film solar cells with 7.6% efficiency, *Nat. Commun.*, 2018, **9**, 2179.
- 27 L. Guo, S. N. Vijayaraghavan, X. Duan, H. G. Menon, J. Wall, L. Kong, S. Gupta, L. Li and F. Yan, Stable and efficient  $\text{Sb}_2\text{Se}_3$  solar cells with solution-processed  $\text{NiO}_x$  hole-transport layer, *Sol. Energy*, 2021, **218**, 525–531.
- 28 R. Tang, S. Chen, Z. Zheng, Z. Su, J. Luo, P. Fan, X. Zhang, J. Tang and G. Liang, Heterojunction annealing enabling record open-circuit voltage in antimony triselenide solar cells, *Adv. Mater.*, 2022, **34**, 2109078.
- 29 S. Dong, L. Sun and F. Yue, Influence of selenium growth condition on the photovoltaic conversion efficiency of  $\text{Sb}_2\text{Se}_3$  as the solar cell absorption layer, *J. Mater. Sci.: Mater. Electron.*, 2022, **33**, 10335–10342.
- 30 W. Shockley and H. J. Queisser, Detailed balance limit of efficiency of p–n junction solar cells, *J. Appl. Phys.*, 1961, **32**, 510–519.
- 31 K. Shen, C. Ou, T. Huang, H. Zhu, J. Li, Z. Li and Y. Mai, Mechanisms and modification of nonlinear shunt leakage in  $\text{Sb}_2\text{Se}_3$  thin film solar cells, *Sol. Energy Mater. Sol. Cells*, 2018, **186**, 58–65.
- 32 M. Lamba, Y. Singh, K. K. Maurya and V. N. Singh, A review on properties, applications, and deposition techniques of antimony selenide, *Sol. Energy Mater. Sol. Cells*, 2021, **230**, 111223.
- 33 A. Basak and U. P. Singh, Numerical modelling and analysis of earth abundant  $\text{Sb}_2\text{S}_3$  and  $\text{Sb}_2\text{Se}_3$  based solar cells using SCAPS-1D, *Sol. Energy Mater. Sol. Cells*, 2021, **230**, 111184.
- 34 F. Baig, Y. H. Khattak, S. Beg and B. M. Soucase, Numerical analysis of a novel CNT/ $\text{Cu}_2\text{O}/\text{Sb}_2\text{Se}_3/\text{In}_2\text{S}_3/\text{ITO}$  antimony selenide solar cell, *Optik*, 2019, **197**, 163107.
- 35 M. Lamba, K. K. Maurya and V. N. Singh, Efficient  $\text{Sb}_2\text{Se}_3$  solar cell with a higher fill factor: A theoretical approach based on thickness and temperature, *Sol. Energy*, 2021, **230**, 803–809.
- 36 S. R. A. Ahmed, A. Sunny and S. Rahman, Performance enhancement of  $\text{Sb}_2\text{Se}_3$  solar cell using a back surface field layer: A numerical simulation approach, *Sol. Energy Mater. Sol. Cells*, 2021, **221**, 110919.
- 37 A. Sunny and S. R. A. Ahmed, Numerical simulation and performance evaluation of highly efficient  $\text{Sb}_2\text{Se}_3$  solar cell with tin sulfide as hole transport layer, *Phys. Status Solidi B*, 2021, **258**, 2000630.
- 38 S. Akin, N. Arora, S. M. Zakeeruddin, M. Grätzel, R. H. Friend and M. I. Dar, New strategies for defect passivation in high-efficiency perovskite solar cells, *Adv. Energy Mater.*, 2020, **10**, 1903090.
- 39 Y.-D. Luo, R. Tang, S. Chen, J.-G. Hu, Y.-K. Liu, Y.-F. Li, X.-S. Liu, Z.-H. Zheng, Z.-H. Su, X.-F. Ma, P. Fan, X.-H. Zhang, H.-L. Ma, Z.-G. Chen and G.-X. Liang, An effective combination reaction involved with sputtered and selenized Sb precursors for efficient  $\text{Sb}_2\text{Se}_3$  thin film solar cells, *Chem. Eng. J.*, 2020, **393**, 124599.
- 40 S. Chen, X. Hu, J. Tao, J. Xue, G. Weng, J. Jiang, X. Shen and S. Chen, Effects of substrate temperature on material and photovoltaic properties of magnetron-sputtered  $\text{Sb}_2\text{Se}_3$  thin films, *Appl. Opt.*, 2019, **58**, 2823–2827.
- 41 M. P. Benavides, S. M. Gallego and M. L. Tomaro, Cadmium toxicity in Plants, *Braz. J. Plant Physiol.*, 2005, **17**, 21–34.
- 42 J. Godt, F. Scheidig, C. G. Siestrup, V. Esche, P. Brandenburg, A. Reich and D. A. Groneberg, The toxicity of cadmium and resulting hazards for human health, *J. Occup. Med. Toxicol.*, 2006, **1**, 22.
- 43 G.-X. Liang, X.-H. Zhang, H.-L. Ma, J.-G. Hu, B. Fan, Z.-K. Luo, Z.-H. Zheng, J.-T. Luo and P. Fan, Facile preparation and enhanced photoelectrical performance of  $\text{Sb}_2\text{Se}_3$  nano-rods by magnetron sputtering deposition, *Sol. Energy Mater. Sol. Cells*, 2017, **160**, 257–262.
- 44 T. D. C. Hobson, L. J. Phillips, O. S. Hutter, H. Shiel, J. E. N. Swallow, C. N. Savory, P. K. Nayak, S. Mariotti, B. Das, L. Bowen, L. A. H. Jones, T. J. Featherstone, M. J. Smiles, M. A. Farnworth, G. Zoppi, P. K. Thakur, T.-L. Lee, H. J. Snaith, C. Leighton, D. O. Scanlon, V. R. Dhanak, K. Durose, T. D. Veal and J. D. Major, Isotype heterojunction solar cells using n-type  $\text{Sb}_2\text{Se}_3$  thin films, *Chem. Mater.*, 2020, **32**, 2621–2630.
- 45 K. Yang, B. Li and G. Zeng, Effects of substrate temperature and  $\text{SnO}_2$  high resistive layer on  $\text{Sb}_2\text{Se}_3$  thin film solar cells prepared by pulsed laser deposition, *Sol. Energy Mater. Sol. Cells*, 2020, **208**, 110381.
- 46 S. Tripathi, B. Kumar and D. K. Dwivedi, Numerical simulation of non-toxic  $\text{In}_2\text{S}_3/\text{SnS}_2$  buffer layer to enhance CZTS solar cells efficiency by optimizing device parameters, *Optik*, 2021, **227**, 166087.
- 47 M. S. Reza, M. F. Rahman, A. Kuddus, M. K. A. Mohammed, D. Pal, A. Ghosh, M. R. Islam, S. Bhattarai, I. A. Shaaban and M. Amami, Design and optimization of high-performance novel  $\text{RbPbBr}_3$ -based solar cells with wide-band-gap s-chalcogenide electron transport layers (ETLs), *ACS Omega*, 2024, **9**, 19824–19836.



- 48 M. Haghighi, M. Minbashi, N. Taghavinia, D.-H. Kim, S. M. Mahdavi and A. A. Kordbacheh, A modeling study on utilizing SnS<sub>2</sub> as the buffer layer of CZT(S, Se) solar cells, *Sol. Energy*, 2018, **167**, 165–171.
- 49 R. K. Gupta and F. Yakuphanoglu, Photoconductive Schottky diode based on Al/p-Si/SnS<sub>2</sub>/Ag for optical sensor applications, *Sol. Energy*, 2012, **86**, 1539–1545.
- 50 J. Yu, C. Xu, F. Ma, S. Hu, Y. Zhang and L. Zhen, Monodisperse SnS<sub>2</sub> nanosheets for high-performance photocatalytic hydrogen generation, *ACS Appl. Mater. Interfaces*, 2014, **6**, 22370–22377.
- 51 X. Hu, G. Song, W. Li, Y. Peng, L. Jiang, Y. Xue, Q. Liu, Z. Chen and J. Hu, Phasecontrolled synthesis and photocatalytic properties of SnS, SnS<sub>2</sub> and SnS/SnS<sub>2</sub> heterostructure nanocrystals, *Mater. Res. Bull.*, 2013, **48**, 2325–2332.
- 52 J. C. Park, K. R. Lee, H. Heo, S. Kwon, M. Lee, W. Jeon, S. Jeong and J. Ahn, Vapor transport synthesis of two-dimensional SnS<sub>2</sub> nanocrystals using a SnS<sub>2</sub> precursor obtained from the sulfurization of SnO<sub>2</sub>, *Cryst. Growth Des.*, 2016, **16**, 3884–3889.
- 53 R. Kumari, M. Lamba, R. Kumar and V. N. Singh, SnTe as a BSF enhances the performance of Sb<sub>2</sub>Se<sub>3</sub> based solar cell: A numerical approach, *Heliyon*, 2022, **8**, e12043.
- 54 Z. Li, M. Ni and X. Feng, Simulation of the Sb<sub>2</sub>Se<sub>3</sub> solar cell with a hole transport layer, *Mater. Res. Express*, 2020, **7**, 16416.
- 55 Y. Ma, B. Tang, W. Lian, C. Wu, X. Wang, H. Ju, C. Zhu, F. Fan and T. Chen, Efficient defect passivation of Sb<sub>2</sub>Se<sub>3</sub> film by tellurium doping for high performance solar cells, *J. Mater. Chem. A*, 2020, **8**, 6510–6516.
- 56 A. Amin, L. Guo, S. N. Vijayaraghavan, D. Li, X. Duan, H. G. Menon, J. Wall, S. Gupta, M. M. Cheng, Y. Zheng, L. Li and F. Yan, Solution-processed vanadium oxides as a hole-transport layer for Sb<sub>2</sub>Se<sub>3</sub> thin-film solar cells, *Sol. Energy*, 2022, **231**, 1–7.
- 57 J. Zhang, R. Kondrotas, S. Lu, C. Wang, C. Chen and J. Tang, Alternative back contacts for Sb<sub>2</sub>Se<sub>3</sub> solar cells, *Sol. Energy*, 2019, **182**, 96–101.
- 58 J. Zhou, X. Zhang, H. Chen, Z. Tang, D. Meng, K. Chi, Y. Cai, G. Song, Y. Cao and Z. Hu, Dual-function of CdCl<sub>2</sub> treated SnO<sub>2</sub> in Sb<sub>2</sub>Se<sub>3</sub> solar cells, *Appl. Surf. Sci.*, 2020, **534**, 147632.
- 59 S. Gohri, J. Madan, R. Pandey and R. Sharma, Performance analysis for SnS- and Sn<sub>2</sub>S<sub>3</sub>-based back surface field CZTSSe solar cell: A simulation study, *J. Electron. Mater.*, 2021, **50**, 6318–6328.
- 60 Z. Benbouzid, W. Benstaali, W. L. Rahal, N. Hassini, M. R. Benzidane and A. Boukourt, Efficiency enhancement by BSF optimization on Cu(In<sub>1-x</sub>, Ga<sub>x</sub>)Se<sub>2</sub> solar cells with tin (IV) sulfide buffer layer, *J. Electron. Mater.*, 2023, **52**, 4575–4586.
- 61 M. Minbashi, A. Ghobadi, M. H. Eshani, H. R. Dizaji and N. Memarian, Simulation of high efficiency SnS-based solar cells with SCAPS, *Sol. Energy*, 2018, **176**, 520–525.
- 62 P. Sinsermsuksakul, J. Heo, W. Noh, A. S. Hock and R. G. Gordon, Atomic layer deposition of tin monosulfide thin films, *Adv. Energy Mater.*, 2011, **1**, 1116–1125.
- 63 Y. Kawano, J. Chantana and T. Minemoto, Impact of growth temperature on the properties of SnS film prepared by thermal evaporation and its photovoltaic performance, *Curr. Appl. Phys.*, 2015, **15**, 897–901.
- 64 M. Patel and A. Ray, Evaluation of back contact in spray deposited SnS thin film solar cells by impedance analysis, *ACS Appl. Mater. Interfaces*, 2014, **6**, 10099–10106.
- 65 D. Lim, H. Suh, M. Suryawanshi, G. Y. Song, J. Y. Cho, J. H. Kim, J. H. Jang, C. W. Jeon, A. Cho, S. Ahn and J. Heo, Kinetically controlled growth of phase-pure SnS absorbers for thin film solar cells: Achieving efficiency near 3% with long-term stability using an SnS/CdS heterojunction, *Adv. Energy Mater.*, 2018, **8**, 1702605.
- 66 S. Hadke, M. Huang, C. Chen, Y. F. Tay, S. Chen, J. Tang and L. Wong, Emerging chalcogenide thin films for solar energy harvesting devices, *Chem. Rev.*, 2022, **122**, 10170–10265.
- 67 V. Steinmann, R. Jaramillo, K. Hartman, R. Chakraborty, R. E. Brandt, J. R. Poindexter, Y. S. Lee, L. Sun, A. Polizzotti, H. H. Park, R. G. Gordon and T. Buonassisi, 3.88% efficient tin sulfide solar cells using congruent thermal evaporation, *Adv. Mater.*, 2014, **26**, 7488–7492.
- 68 S. Kawanishi, I. Suzuki, S. R. Bauers, A. Zakutayev, H. Shibata, H. Yanagi and T. Omata, SnS homojunction solar cell with n-type single crystal and p-type thin film, *Sol. RRL*, 2021, **5**, 2000708.
- 69 P. Sinsermsuksakul, K. Hartman, S. B. Kim, J. Heo, L. Sun, H. H. Park, R. Chakraborty, T. Buonassisi and R. G. Gordon, Enhancing the efficiency of SnS solar cells via band-offset engineering with a zinc oxysulfide buffer layer, *Appl. Phys. Lett.*, 2013, **102**, 053901.
- 70 M. Messaoudi, M. S. Aida, N. Attaf, T. Bezzi, J. Bougdira and G. Medjahdi, Deposition of tin(II) sulfide thin films by ultrasonic spray pyrolysis: Evidence of sulfur exo-diffusion, *Mater. Sci. Semicond. Process.*, 2014, **17**, 38–42.
- 71 A. Basak, A. Hati, A. Mondal, U. P. Singh and S. K. Taheruddin, Effect of substrate on the structural, optical and electrical properties of SnS thin films grown by thermal evaporation method, *Thin Solid Films*, 2018, **645**, 97–101.
- 72 J. Ullah, Z. U. Rehman, K. Anum, I. Ahmad, T. Ali, K. Hayat and S. K. Shah, First principles calculations of Sb<sub>2</sub>Se<sub>3</sub> and SCAPS-1D simulation-guided optimization for improved photovoltaic properties in solar cells, *Opt. Quantum Electron.*, 2025, **57**, 187.
- 73 D.-B. Li, X. Yin, C. R. Grice, L. Guan, Z. Song, C. Wang, C. Chen, K. Li, A. J. Cimaroli, R. A. Awni, D. Zhao, H. Song, W. Tang, Y. Yan and J. Tang, Stable and efficient CdS/Sb<sub>2</sub>Se<sub>3</sub> solar cells prepared by scalable close space sublimation, *Nano Energy*, 2018, **49**, 346–353.
- 74 E. A. Nyiekaka, T. A. Aika, E. Danladi, C. E. Akhabue and P. E. Orukpe, Simulation and optimization of 30.17% high performance N-type TCO-free inverted perovskite solar cell using inorganic transport materials, *Sci. Rep.*, 2024, **14**, 12024.
- 75 M. M. Rahman, M. H. Ali, M. D. Haque and A. Z. M. T. Islam, Numerical modeling and extensive analysis of an extremely efficient RbGeI<sub>3</sub>-based perovskite



- solar cell by incorporating a variety of ETL and HTL materials to enhance PV performance, *Energy Adv.*, 2024, **3**, 2377–2398.
- 76 M. Burgelman, K. Decock, S. Khelifi and A. Abass, Advanced electrical simulation of thin-film solar cells, *Thin Solid Films*, 2013, **535**, 296–301.
- 77 A. Shakoor, G. A. Nowsherwan, M. F. Aamir, A. Ali, S. U. Rehman, W. Alam, M. Yasir, K. Arif, M. Ahmad and J. Yousaf, Performance evaluation of solar cells by different simulating softwares, *Solar PV Panels - Recent Advances and Future Prospects*, IntechOpen, 2023, vol. 7, pp. 1–21.
- 78 A. A. El-Naggar, A. M. Eid, Y. Rafat, M. A. Khamis, M. Bakry, S. Elkun, W. Ismail, S. W. Sharshir, A. El-Shaer and M. Abdelfatah, SCAPS simulation and design of highly efficient  $\text{CuBi}_2\text{O}_4$ -based thin film solar cells (TFSCs) with hole and electron transport layers, *Sci. Rep.*, 2025, **15**, 28300.
- 79 A. D. Adewoyin, M. A. Olopade, O. O. Oyebola and B. Rilwan, Optimization: a proposed pathway to overcome the impasse of low efficiency in CZTS thin-film photovoltaics, *J. Mater. Sci.: Mater. Electron.*, 2020, **31**, 17585–17593.
- 80 E. N. V. Mercy, A.-D. R. Chettiar, K. Sekar, S. Kandasamy and L. Marasamy, Modeling of (Ca,Ba)ZrS<sub>3</sub> solar cells with next-gen spinel hole transport layers via SCAPS-1D, *Opt. Quantum Electron.*, 2025, **57**, 311.
- 81 M. Burgelman, P. Nollet and S. Degrave, Modelling polycrystalline semiconductor solar cells, *Thin Solid Films*, 2000, **361–362**, 527–532.
- 82 M. Burgelman and K. Gärtner, SCAPS Manual, 2025, <https://www.scaps.elis.ugent.be>.
- 83 A. Saidarsan, S. Guruprasad, A. Malik, P. Basumatary and D. S. Ghosh, A critical review of unrealistic results in SCAPS-1D simulations: causes, practical solutions and roadmap ahead, *Sol. Energy Mater. Sol. Cells*, 2025, **279**, 113230.
- 84 S. Y. Myong, J. Steinhauser, R. Schluchter, S. Fay, E. V. Sauvain, A. Shah, C. Ballif and A. Rufenacht, Temperature dependence of the conductivity in large-grained boron-doped ZnO films, *Sol. Energy Mater. Sol. Cells*, 2007, **91**, 1269–1274.
- 85 L. Et-taya, A. Benami and T. Ouslimane, Study of CZTSSe-based solar cells with different ETMs by SCAPS, *Sustainability*, 2022, **14**, 1916.
- 86 F. Baig, Y. H. Khattak, S. Ullah, B. M. Soucase, S. Beg and H. Ullah, Numerical analysis a guide to improve the efficiency of experimentally designed solar cell, *Appl. Phys. A: Mater. Sci. Process.*, 2018, **124**, 471.
- 87 S. Rahman and S. R. A. Ahmed, Photovoltaic performance enhancement in CdTe thin-film heterojunction solar cell with  $\text{Sb}_2\text{S}_3$  as hole transport layer, *Sol. Energy*, 2021, **230**, 605–617.
- 88 A. Hosen and S. R. A. Ahmed, Performance analysis of SnS solar cell with a hole transport layer based on experimentally extracted device parameters, *J. Alloys Compd.*, 2022, **909**, 164823.
- 89 M. T. Islam, M. Shaikh and A. Kumar, Dual- and triple-absorber solar cell architecture achieves significant efficiency improvements, *J. Comput. Electron.*, 2025, **24**, 27.
- 90 S. Shao and M. A. Loi, The role of the interfaces in perovskite solar cells, *Adv. Mater. Interfaces*, 2020, **7**, 1901469.
- 91 P. Bhattacharjee, R. Garain, A. Basak and U. P. Singh, Numerical modelling and performance evaluation of SnS based heterojunction solar cell with p+-SnS BSF layer, *Opt. Quantum Electron.*, 2022, **54**, 867.
- 92 B. Sultana, A. T. M. S. Islam, M. D. Haque, A. Kuddus, M. H. Ali and M. F. Rahman, Numerical study of  $\text{MoSe}_2$ -based dual-heterojunction with  $\text{In}_2\text{Te}_3$  BSF layer toward high-efficiency photovoltaics, *Phys. Scr.*, 2023, **98**, 095935.
- 93 S. Maqsood, Z. Ali, K. Ali, R. B. Awan, Y. Arooj and A. Younus, Optimization of CdS-free non-toxic electron transport layer for  $\text{Sb}_2\text{S}_3$ -based solar cell with notable enhanced performance, *J. Comput. Electron.*, 2023, **22**, 1715–1724.
- 94 Z. R. Abdulghani, A. S. Najm, A. M. Holi, A. A. Al-Zahrani, K. S. Al-Zahrani and H. Moria, Numerical simulation of quantum dots as a buffer layer in CIGS solar cells: A comparative study, *Sci. Rep.*, 2022, **12**, 8099.
- 95 M. Abdelfatah, A. M. E. Sayed, W. Ismail, S. Ulrich, V. Sittinger and A. El-Shaer, SCAPS simulation of novel inorganic  $\text{ZrS}_2/\text{CuO}$  heterojunction solar cells, *Sci. Rep.*, 2023, **13**, 4553.
- 96 W. M. M. Lin, N. Yazdani, O. Yarema, S. Volk, M. Yarema, T. Kirchartz and V. Wood, Simulating nanocrystal-based solar cells: A lead sulfide case study, *J. Chem. Phys.*, 2019, **151**, 241104.
- 97 A. Bouarissa, A. Gueddim, N. Bouarissa and H. Maghraoui-Meherezi, Modeling of  $\text{ZnO}/\text{MoS}_2/\text{CZTS}$  photovoltaic solar cell through window buffer and absorber layers optimization, *Mater. Sci. Eng., B*, 2021, **263**, 114816.
- 98 M. A. Rahman, Enhancing the photovoltaic performance of Cd-free  $\text{Cu}_2\text{ZnSnS}_4$  heterojunction solar cells using SnS HTL and  $\text{TiO}_2$  ETL, *Sol. Energy*, 2021, **215**, 64–76.
- 99 Z.-P. Huang, Y.-X. Chen, Z.-H. Huang, W.-W. Lin, Y. Mao, L.-M. Lin, L.-Q. Yao, H. Li, L.-P. Cai and G.-L. Chen, Simulation of highly efficient GeSe-based solar cells with SCAPS-1D, *Heliyon*, 2023, **9**, e18776.
- 100 W. Henni, W. L. Rahal and D. Rached, Path toward high-efficiency CZTS solar cells with buffer layer optimization, *Acta Phys. Pol. A*, 2022, **142**, 445–449.
- 101 X. Hao, K. Sun, C. Yan, F. Liu, J. Huang, A. Pu and M. Green, Large  $V_{OC}$  improvement and 9.2% efficient pure sulfide  $\text{Cu}_2\text{ZnSnS}_4$  solar cells by heterojunction interface engineering, in *2016 IEEE 43rd Photovoltaic Specialists Conference (PVSC)*, Portland, OR, USA, 2016, pp. 2164–2168.
- 102 M. A. H. Pappu, A. Kuddus, B. K. Mondal, A. T. Abir and J. Hossain, Design of n-CdS/p-CuInTe<sub>2</sub>/p + -MoS<sub>2</sub> thin film solar cell with a power conversion efficiency of 34.32%, *Opt. Continuum*, 2023, **2**, 942–955.
- 103 H. A. Mohamed, Optimized conditions for the improvement of thin film CdS/CdTe solar cells, *Thin Solid Films*, 2015, **589**, 72–78.



- 104 S. Dabbabi, T. B. Nasr and N. K. Turki, Parameters optimization of CIGS solar cell using 2D physical modeling, *Results Phys.*, 2017, 7, 4020–4024.
- 105 A. Isha, A. Kowsar, A. Kuddus, M. K. Hossain, M. H. Ali, M. D. Haque and M. F. Rahman, High efficiency  $\text{Cu}_2\text{MnSnS}_4$  thin film solar cells with SnS BSF and CdS ETL layers: A numerical simulation, *Heliyon*, 2023, 9, e15716.
- 106 O. Astakhov, V. Smirnov, R. Carius, B. E. Pieters, Y. Petrusenko, V. Borysenko and F. Finger, Relationship between absorber layer defect density and performance of a-Si: H and  $\mu\text{-Si}$ : H solar cells studied over a wide range of defect densities generated by 2 MeV electron bombardment, *Sol. Energy Mater. Sol. Cells*, 2014, 129, 17–31.
- 107 B. K. Mondal, S. K. Mostaque and J. Hossain, Theoretical insights into a high-efficiency  $\text{Sb}_2\text{Se}_3$ -based dual-heterojunction solar cell, *Heliyon*, 2022, 8, e09120.
- 108 M. A. Monnaf, A. K. M. M. Haque, M. H. Ali, S. Bhattarai, M. D. Haque and M. F. Rahman, Design and simulation of  $\text{Cu}_2\text{SnSe}_3$ -based solar cells using various hole transport layer (HTL) for performance efficiency above 32%, *Phys. Scr.*, 2023, 98, 125903.
- 109 M. Matys, R. Stoklas, J. Kuzmik, B. Adamowicz, Z. Yatabe and T. Hashizume, Characterization of capture cross sections of interface states in dielectric/III-nitride heterojunction structures, *J. Appl. Phys.*, 2016, 119, 205304.
- 110 A. T. Ngoupo and J. M. B. Ndjaka, Performance enhancement of  $\text{Sb}_2\text{Se}_3$ -based solar cell with hybrid buffer layer and  $\text{MoSe}_2$  as a hole transport material using simulator device, *Discover Mech. Eng.*, 2022, 1(1), 5.
- 111 M. M. Khatun, A. Hosen and S. R. A. Ahmed, Evaluating the performance of efficient  $\text{Cu}_2\text{NiSnS}_4$  solar cell—A two stage theoretical attempt and comparison to experiments, *Heliyon*, 2023, 9, e20603.
- 112 N. K. Bansal, S. Porwal, H. Dixit, D. Kumar and T. Singh, A theoretical study to investigate the impact of bilayer interfacial modification in perovskite solar cell, *Energy Technol.*, 2023, 11, 2201395.
- 113 M. M. Khatun, A. Sunny and S. R. A. Ahmed, Numerical investigation on performance improvement of  $\text{WS}_2$  thin-film solar cell with copper iodide as hole transport layer, *Sol. Energy*, 2021, 224, 956–965.
- 114 S. Ahmmmed, A. Aktar, J. Hossain and A. B. M. Ismail, Enhancing the open circuit voltage of the SnS based heterojunction solar cell using NiO HTL, *Sol. Energy*, 2020, 207, 693–702.
- 115 A. Raj, M. Kumar, A. Kumar, A. Laref and A. Anshul, Investigating the potential of lead-free double perovskite  $\text{Cs}_2\text{AgBiBr}_6$  material for solar cell applications: A theoretical study, *Int. J. Energy Res.*, 2022, 46, 13801–13819.
- 116 K. Chakraborty, M. G. Choudhury and S. Paul, Numerical study of  $\text{Cs}_2\text{TiX}_6$  ( $\text{X} = \text{Br}^-$ ,  $\text{I}^-$ ,  $\text{F}^-$  and  $\text{Cl}^-$ ) based perovskite solar cell using SCAPS-1D device simulation, *Sol. Energy*, 2019, 194, 886–892.
- 117 R. Hosen, S. Sikder, M. S. Uddin, M. M. Haque, H. Mamur and M. R. A. Bhuiyan, Effect of various layers on improving the photovoltaic efficiency of  $\text{Al/ZnO/CdS/CdTe/Cu}_2\text{O/Ni}$  solar cells, *Alloys Metall. Syst*, 2023, 4, 100041.
- 118 R. A. Street, M. Schoendorf, A. Roy and J. H. Lee, Interface state recombination in organic solar cells, *Phys. Rev. B*, 2010, 81, 205307.
- 119 F. F. Muhammad, M. Y. Yahya, S. S. Hameed, F. Aziz, K. Sulaiman, M. A. Rasheed and Z. Ahmad, Employment of single-diode model to elucidate the variations in photovoltaic parameters under different electrical and thermal conditions, *PLoS One*, 2017, 12, e0182925.
- 120 J. Hossain, M. M. A. Moon, B. K. Mondal and M. A. Halim, Design guidelines for a highly efficient high-purity germanium (HPGe)-based doubleheterojunction solar cell, *Opt Laser. Technol.*, 2021, 143, 107306.
- 121 A. Kumar, R. T. Prabu and A. Das, Configuration analysis of SnS based solar cells for high-efficiency devices, *Opt. Quantum Electron.*, 2022, 54, 521.
- 122 M. Al-Hattab, L. Moudou, M. Khenfouch, O. Bajjou, Y. Chrafi and K. Rahmani, Numerical simulation of a new heterostructure CIGS/GaSe solar cell system using SCAPS-1D software, *Sol. Energy*, 2021, 227, 13–22.
- 123 A. Kuddus, A. B. M. Ismail and J. Hossain, Design of a highly efficient CdTe-based dual-heterojunction solar cell with 44% predicted efficiency, *Sol. Energy*, 2021, 221, 488–501.
- 124 B. K. Mondal, S. K. Mostaque, M. A. Rashid, A. Kuddus, H. Shirai and J. Hossain, Effect of CdS and  $\text{In}_3\text{Se}_4$  BSF layers on the photovoltaic performance of PEDOT:PSS/n-Si solar cells: simulation based on experimental data, *Superlattices Microstruct.*, 2021, 152, 106853.
- 125 J. Hossain, B. K. Mondal and S. K. Mostaque, Computational investigation on the photovoltaic performance of an efficient GeSe-based dual-heterojunction thin film solar cell, *Semicond. Sci. Technol.*, 2022, 37, 015008.
- 126 M. S. Chowdhury, S. A. Shahahmadi, P. Chelvanathan, S. K. Tiong, N. Amin, K. Techato, N. Nuthammachot, T. Chowdhury and M. Suklueng, Effect of deep-level defect density of the absorber layer and n/i interface in perovskite solar cells by SCAPS-1D, *Results Phys.*, 2020, 16, 102839.
- 127 X. Liu, Y. Qiao, Y. Liu, J. Liu, E. Jia, S. Chang, X. Shen, S. Li and K. Cheng, Enhanced open circuit voltage of  $\text{Sb}_2\text{Se}_3/\text{CdS}$  solar cells by annealing Se-rich amorphous  $\text{Sb}_2\text{Se}_3$  films prepared via sputtering process, *Sol. Energy*, 2020, 195, 697–702.
- 128 R. Tang, X. Chen, G. Liang, Z. Su, J. Luo and P. Fan, Magnetron sputtering deposition and selenization of  $\text{Sb}_2\text{Se}_3$  thin film for substrate  $\text{Sb}_2\text{Se}_3/\text{CdS}$  solar cells, *Surf. Coat. Technol.*, 2019, 360, 68–72.
- 129 X. Hu, J. Tao, Y. Wang, J. Xue, G. Weng, C. Zhang, S. Chen, Z. Zhu and J. Chu, 5.91%-efficient  $\text{Sb}_2\text{Se}_3$  solar cells with a radio-frequency magnetron-sputtered CdS buffer layer, *Appl. Mater. Today*, 2019, 16, 367–374.
- 130 K. Li, S. Wang, C. Chen, R. Kondrotas, M. Hu, S. Lu, C. Wang, W. Chen and J. Tang, 7.5% n-i-p  $\text{Sb}_2\text{Se}_3$  solar



## Paper

- cells with CuSCN as a hole-transport layer, *J. Mater. Chem. A*, 2019, **7**, 9665–9672.
- 131 I. Gharibshahian, A. A. Orouji and S. Sharbati, Towards high efficiency Cd Free  $\text{Sb}_2\text{Se}_3$  solar cells by the band alignment optimization, *Sol. Energy Mater. Sol. Cells*, 2020, **212**, 110581.
- 132 F. Baig, Y. H. Khattak, A. Shuja, K. Riaz and B. M. Soucase, Performance investigation of  $\text{Sb}_2\text{Se}_3$  based solar cell by device optimization, band offset engineering and hole transport layer in SCAPS-1D, *Curr. Appl. Phys.*, 2020, **20**, 973–981.
- 133 Y. Cao, X. Zhu, H. Chen, X. Zhang, J. Zhou, Z. Hu and J. Pang, Towards high efficiency inverted  $\text{Sb}_2\text{Se}_3$  thin film solar cells, *Sol. Energy Mater. Sol. Cells*, 2019, **200**, 109945.

